buildings

MDPI

Article

Field Validation of Nonlinear Dynamic Simulation for Plan-Irregular RC Buildings: Insights from the 2024 Hualien Earthquake

Ying-Chuan Chen [1], Kuo-Hung Chao [1], Yu-Chi Sung [1,*] and Jin-Sheng Lin [2]

[1] Department of Civil Engineering, National Taipei University of Technology, Taipei 106344, Taiwan
[2] Maoxin Engineering Consultants Co., Ltd., Hualien City 970020, Taiwan
* Correspondence: sungyc@ntut.edu.tw

Abstract

This study evaluates the post-earthquake damage of a 17-story plan-irregular reinforced concrete (RC) building damaged during the 2024 Hualien earthquake. A three-dimensional numerical model was constructed in ETABS, utilizing nonlinear component characteristics derived from the mechanics-based Seismic Evaluation of RC Building (SERCB) framework to execute nonlinear dynamic time-history analysis (NDTHA). The actual triaxial ground motion records from the 3 April 2024 earthquake were applied as the seismic input. To correlate analytical outcomes with physical seismic damage, a displacement-based ductility development index (D) was adopted to quantitatively associate simulated plastic hinge responses with field-observed damage states ranging from Slight (DS I) to Collapse (DS V). Post-earthquake reconnaissance revealed that structural damage was primarily concentrated in the perimeter RC shear walls between the 1st and 6th stories. The predicted wall damage states spanned from Moderate (DS II) to Severe (DS IV), whereas the primary beam–column frame exhibited only Slight damage (DS I). Quantitative comparison demonstrates exact damage state match rates of 63.6% (7/11) for Frame 1 and 71.4% (5/7) for Frame 2, with all remaining discrepancies bounded within a minor one-class margin. These analytical results show high consistency with field observations, confirming that NDTHA incorporating SERCB-based plastic hinge modeling can effectively reproduce the nonlinear seismic behavior and localized damage distribution of torsionally irregular RC structures. The findings extend traditional laboratory-scale component validation to full-scale building damage reconnaissance, providing robust empirical evidence for cross-validating physical seismic damage against dynamic simulation predictions.

Keywords: damage state; building damage; plastic hinge; component ductility

Check for updates

Academic Editor: Emanuele Brunesi

Received: 13 July 2026
Revised: 16 August 2026
Accepted: 21 August 2026
Published: 26 August 2026

Copyright: © 2026 by the authors. Licensee MDPI, Basel, Switzerland. This article is an open access article distributed under the terms and conditions of the Creative Commons Attribution (CC BY) license.

1. Introduction

Taiwan is situated at the convergent boundary between the Philippine Sea and Eurasian plates. This tectonic setting drives high seismic activity, with the highest seismic hazard concentrated in the southwestern zone and the eastern Longitudinal Valley [1]. Statistical data from the Central Weather Administration (CWA) between 2016 and early 2026 indicate that Taiwan experiences an average of 153.6 felt earthquakes annually [2]. Within this period, seismic events exceeding a local magnitude (ML) of 6.0 occur at an average frequency of 5.7 times per year, reflecting intense crustal activity within the region.

Historical earthquakes in Taiwan highlight the decisive impact of seismic design and construction quality on structural performance. Regarding the 1999 Chi-Chi earthquake,

Tsai et al. [3] identified soft-story and short-column shear failures as primary failure modes, while Su et al. [4] and Naeim et al. [5] attributed building collapses to substandard concrete, improper rebar splicing, and inadequate transverse reinforcement. Following the Chi-Chi event, Henry et al. [6] noted that revised seismic codes and systematic public retrofits effectively mitigated structural risks. Subsequently, Zepeda and Hagen [7] observed during the 2016 Meinong earthquake that member configurations and design details directly governed seismic performance. Furthermore, during the 2018 Hualien earthquake, Wang [8] and Ji et al. [9] demonstrated that near-fault velocity pulses impose severe impulsive demands over short durations, significantly amplifying the structural damage of soft-story RC buildings.

On 3 April 2024, at 07:58 (GMT+8), an earthquake with a local magnitude (ML) of 7.2 struck the eastern offshore region of Taiwan at a focal depth of approximately 19.7 km, with its epicenter located near Hualien County [10]. The Heping station in Hualien recorded a maximum peak ground acceleration (PGA) exceeding 440 gal (Intensity 6-Strong), and numerous strong-motion stations nationwide captured ground motions with PGAs exceeding 80 gal (Intensity 5 and above). These records classify this event as one of the most representative strong earthquakes in recent years, which induced extensive structural damage throughout the Hualien area. Post-earthquake reconnaissance by Chuang et al. [11] indicated that high-rise and soft-story buildings sustained the most significant damage, with common failure modes encompassing shear wall cracking, column element failure, and localized collapse. Their study further revealed the interaction between near-fault ground motion characteristics and building configurations, highlighting the critical impact of design detailing and construction quality on seismic performance [12].

Post-earthquake field investigations provide essential empirical evidence for evaluating the seismic performance of existing structures and for validating analytical models against observed damage. Nonlinear dynamic time-history analysis (NDTHA) provides a direct means of evaluating the inelastic response of structures subjected to earthquake ground motions [13]. Nascimbene [14] demonstrated the applicability of distributed-plasticity (fiber-based) models for representing nonlinear dynamic behavior and calibrating input ground motions in experimental studies. Tu et al. [15] evaluated a simplified nonlinear static procedure using 31 earthquake-damaged school buildings affected by the 1999 Chi-Chi earthquake and demonstrated its applicability for estimating structural capacity. Yang et al. [16] further developed a high-fidelity finite element model incorporating soil–structure interaction for a 12-story RC building subjected to the 1994 Northridge earthquake, with comparisons between numerical results and CSMIP station records providing evidence for the applicability of detailed numerical models in full-scale structural assessment.

Recent earthquake reconnaissance has further demonstrated that the seismic performance of RC buildings is strongly influenced by structural configuration, material properties, detailing, and construction-related deficiencies. Cosgun et al. [17] investigated two inactive multi-story RC buildings through field surveys, laboratory testing, and numerical seismic analyses, showing that retrofit-induced increases in structural stiffness could reduce displacement demands while potentially increasing shear-related demands if not appropriately designed. Peker et al. [18] combined post-earthquake observations with seismic performance assessment and strengthening analysis of an RC residential building damaged during the 2023 Türkiye earthquakes, highlighting the importance of structural deficiencies in post-earthquake evaluation. Kocakaplan Sezgin et al. [19] similarly investigated damage to RC buildings following the 2023 Kahramanmaraş earthquakes and emphasized the influence of structural systems, detailing, and construction-related deficiencies on observed damage. Aguayo et al. [20] further showed that plan asymmetry in a 14-story RC building with complex shear walls resulted in substantially different seismic demands between the

two principal directions, highlighting the influence of structural configuration on seismic response. Blasi et al. [21] likewise demonstrated that structural irregularity can lead to variations in displacement and acceleration demands under seismic excitation.

Recent studies have increasingly sought to establish connections between field-observed damage and analytical assessments. Sönmez et al. [22] compared observed building damage following the 2023 Kahramanmaraş earthquakes with fragility-based assessments, providing evidence of the consistency between empirical observations and analytical predictions. Tan et al. [23] investigated a severely damaged substandard RC building and showed that numerical modeling incorporating infill-wall effects could reproduce important features of the observed damage distribution. These studies highlight the value of integrating post-earthquake reconnaissance with analytical approaches for evaluating the seismic performance of existing RC buildings. However, detailed validation of event-specific nonlinear dynamic simulations against actual earthquake damage remains relatively limited. In particular, relatively few case studies have quantitatively compared component-level observed damage with nonlinear analytical responses using strong-motion records from the investigated earthquake.

To address this research gap, this study investigates a 17-story plan-irregular reinforced concrete building damaged during the 2024 Hualien earthquake by comparing documented post-earthquake structural damage states with NDTHA results obtained via ETABS. The nonlinear hinge properties are derived using the mechanics-based SERCB platform rather than relying solely on default software parameters or simplified empirical assumptions. A displacement-based ductility index is further employed to quantitatively correlate the analytical nonlinear responses with field-observed damage states. The numerical results show strong consistency with the observed damage distribution, particularly in the lower-story shear walls. These findings demonstrate the capability of the adopted NDTHA framework, incorporating mechanics-based SERCB plastic hinges, to reproduce the observed damage characteristics of the investigated plan-irregular RC building under site-specific seismic excitation.

2. Case Study Building and Earthquake Damage Overview

2.1. Site Location and Site Geological Conditions

This study focuses on a 17-story reinforced concrete (RC) building located in a high seismic hazard zone in eastern Taiwan. This region is controlled by multiple active faults, including the Milun, Lingding, Ruisui, Qimei, Yuli, and Chihshang faults, resulting in highly frequent seismic activity. The investigated building is situated approximately 1.8 km from the active Milun fault (Figure 1). Located within the near-fault hazard zone, the structure is susceptible to significant near-fault ground motion effects during strong earthquakes.

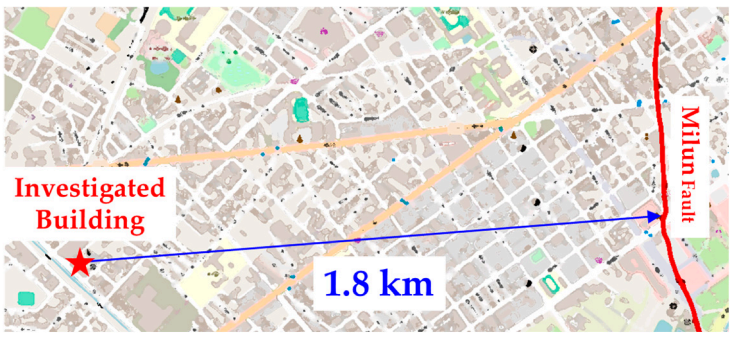

Figure 1. Relative location of the investigated structure and the Milun Fault, adapted from open-source maps provided by the Geology Cloud Value-Added Application Platform, Geological Survey and Mining Management Agency (GSMMA), Ministry of Economic Affairs (MOEA), Taiwan [24].

Due to the lack of original borehole records for the investigated site, geotechnical data from a neighboring borehole located 244 m away (Borehole No. BH-014, Figure 2) were adopted to characterize the subsurface conditions. The stratigraphy predominantly consists of light gray, medium-to-fine sandy gravel, which is intercalated with gray silty sand and fine gravel. Table 1 tabulates the detailed lithological profile.

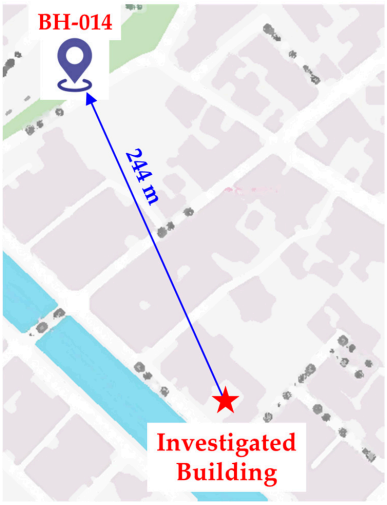

(**a**)

Project Name : -
Location :
Ji'an Township, Hualien County
Borehole No. : BH-014
Total Depth : 40 m

Ground Elevation : 16.95 m
Coordinate System : TWD97
Groundwater : 0 m
N : 2,652,202.00
E : 310,131.39

Drilling Date : Nov.13-17, 2021
Drilling Contractor:
Ying-Ren Engineering Consultants Co., Ltd.

Depth (m)	Water Usage (m³)	Drilling Method	Sample No.	Water Table ∇	SPT N-Value	Legend	Soil / Rock Description	Color	Gravel (%)	Sand (%)	Silt (%)	Clay (%)
0	34	Wireline core drilling	S-1-1	110/11/25	4+6+7		Light gray medium-to-fine sandy gravel	Gray	1	81	16	1
2					17+36+64/3							
4					22+100/3							
6					25+23+100/7							
8					100							
10												
12					100/10							
14												
16					100/9							
18					36+64/5							
20					39+61/8							
22												
24					33+67/4		25 m					
26			S-11-2		11+15+17		Gray silty sand with gravel and fine gravel		2	76	19	3
28												
30	34	Wireline core drilling	S-12-2		14+17+18				2	72	22	4
32			S-13-1		13+16+18		33.7 m	Gray	0	1	91	8
34							Gray silty sandy gravel 34.1 m					
36			S-14-2		16+18+20				0	1	81	18
38							Gray silty sand with gravel and fine gravel 40 m					
40			S-15-2		17+20+23				0	0	84	16

(**b**)

Figure 2. Engineering borehole report (BH-014): (**a**) Location map of the referenced borehole; (**b**) geological borehole column, sourced from the Engineering Geological Investigation Database, GSMMA, MOEA [25].

Table 1. Soil profiles.

No	Layer	Thickness (m)	Depth (m)
1	Light gray, medium-to-fine sandy gravel	25	25.0
2	Gray, silty sand with gravel and fine gravel	8.7	33.7
3	Gray, silty sandy gravel	0.4	34.1
4	Gray, silty sand with gravel and fine gravel	5.9	40.0

Note: Compiled from data provided by the Engineering Geological Investigation Database, GSMMA, MOEA [25].

Standard Penetration Test (SPT) profiles were analyzed to evaluate the stiffness of the bearing stratum, as summarized in Table 2. The empirical records indicate that the gravelly sand layer consistently reached the refusal blow count of N = 100, confirming high skeletal stiffness of the soil. The time-averaged shear wave velocity in the top 30 m (V_{s30}) of the site was 381.4 m/s. According to the Taiwan Seismic Design Code for Buildings, a site with V_{s30} > 270 m/s is classified as a Class I site (stiff ground or rock).

Table 2. SPT N-value and shear wave velocity.

No	Soil Thickness d (m)	SPT N-Value	V_s	d/V_s
1	1.5	17	205.703	0.00729
2	1.5	100	371.327	0.00404
3	2	100	371.327	0.00539
4	2	100	371.327	0.00539
5	2	100	371.327	0.00539
6	2	100	371.327	0.00539
7	2	100	371.327	0.00539
8	2	100	371.327	0.00539
9	2	100	371.327	0.00539
10	3	100	371.327	0.00808
11	2	100	464.159	0.00431
12	2	100	464.159	0.00431
13	2	100	464.159	0.00431
14	2	100	464.159	0.00431
15	2	100	464.159	0.00431

Note: Borehole stratigraphy and SPT-N values were obtained from the Engineering Geological Investigation Database (GSMMA, MOEA) [25]. Shear wave velocities (Vs) were calculated in accordance with the 2024 Building Seismic Design Code and Commentary of Taiwan [26].

2.2. Building Configuration and Geometry

This study investigates a 17-story RC building constructed in 1995 as the target structure (Figure 3). The structural configuration comprises 17 stories above ground and 1 basement level. The ground floor has a clear height of 3.2 m, and the typical stories are 2.9 m high, resulting in a total structural height of 49.6 m above ground. The cumulative floor area of this specific building is 14,697 m^2.

The structural plan layout and member dimensions of the investigated building are illustrated in Figure 4 and Table 3, respectively. The building features a C-shaped configuration composed of four interconnected structural units, introducing a notable eccentricity between the center of mass (CM) and center of rigidity (CR). Consequently, seismic ground motions induce pronounced translational–torsional coupling, which substantially amplifies lateral deformation and shear force demands on the perimeter boundary members.



Figure 3. Post-earthquake photographic documentation of the investigated building: (**a**) front view, (**b**) rear view, (**c**) left-side view, and (**d**) right-side view.

Table 3. Summary of structural component dimensions.

Type	No.	Size (cm)	Type	No.	Size (cm)
Column	C1	60 × 150	Beam	G1, G2	50 × 70
	C2	40 × 100		G3, G4	70 × 70
	C3	90 × 90		G5~G8	50 × 70
	C4	40 × 100		G9	40 × 70
	C5	40 × 100		G10	50 × 70
	C6	60 × 130		G11~G13	40 × 70
	C7~C10	90 × 90		G14~G20	50 × 70
	C11	150 × 60		CG1	50 × 70
	C12	90 × 90		cb1	30 × 60
	C14	90 × 90		b1, b2, b4	30 × 50
Slab	S0	T = 20		b3, b5	30 × 55
	S1~S6	T = 15		b6, b7~b10	30 × 60
	CS1	T = 15		b6A	40 × 60

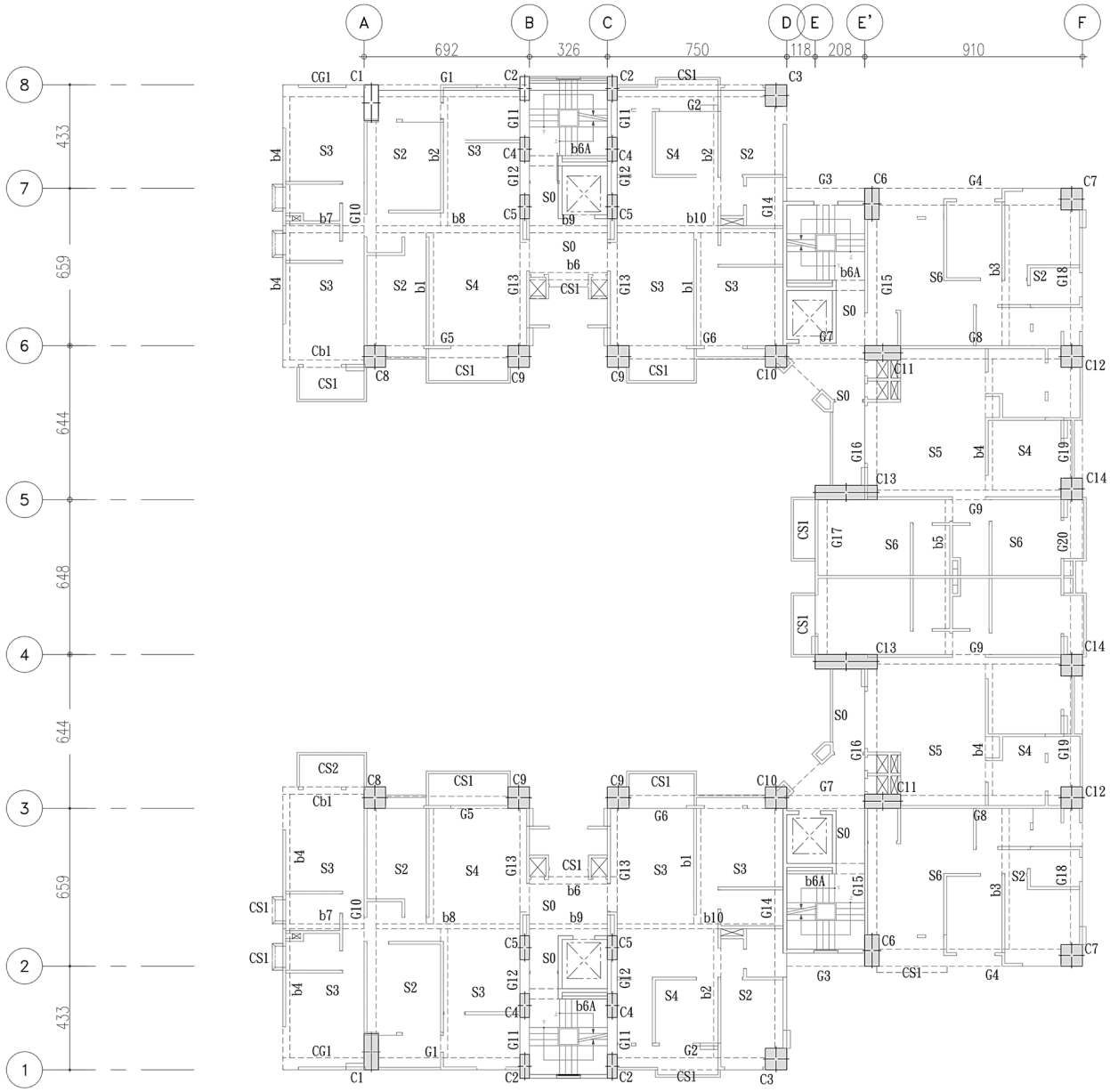

Figure 4. Typical structural plan configuration of the investigated building (Grid lines 1–8 and A–F denote the structural framing axes in the transverse and longitudinal directions, respectively).

2.3. Structural System and Design Details

The lateral force-resisting system of the building comprises an RC moment-resisting frame combined with structural shear walls positioned around the elevator shafts on both flanks, which classifies the structure as a frame-shear wall dual system. The structural shear walls have a thickness of 20 cm. The remaining RC walls serve as peripheral exterior walls and partitions, while specific internal partitions consist of 11 cm thick masonry walls. At the ground level, the primary beam sections have dimensions of 40 × 70 cm and 50 × 70 cm (Figure 5), whereas the column cross-sections measure 60 × 150 cm, 40 × 100 cm, and 90 × 90 cm (Figure 6). Regarding reinforcement detailing, the RC wall thicknesses vary across 12, 15, and 20 cm; specifically, a single layer of reinforcement is arranged in the 12 cm walls, whereas two-way double layers are implemented in both the 15 cm and 20 cm walls (Figure 7).

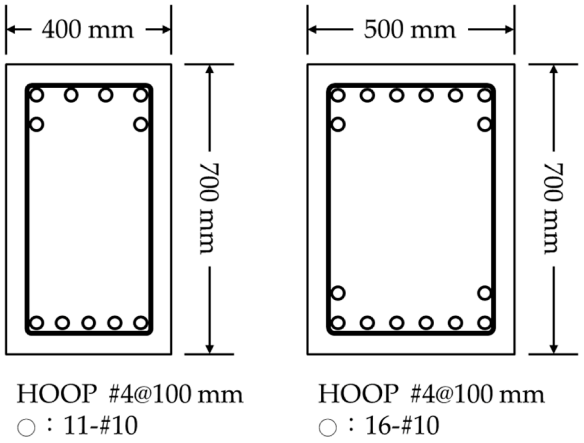

Figure 5. Cross-sectional dimensions and reinforcement details of the primary beams.

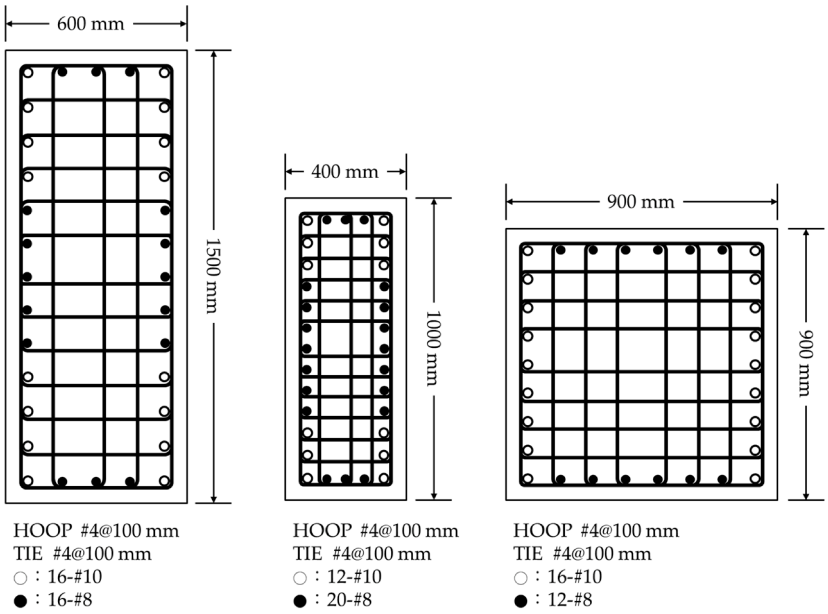

Figure 6. Cross-sectional dimensions and reinforcement details of the primary columns.

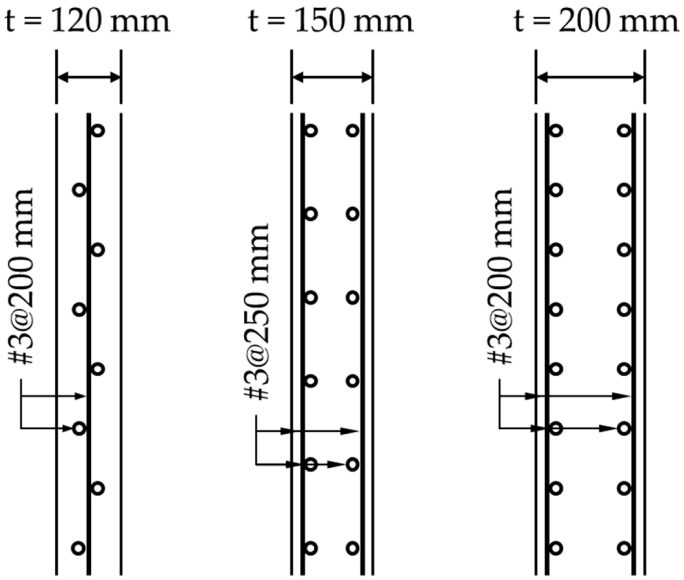

Figure 7. Reinforcement details of the RC walls featuring single and double curtains.

Regarding the foundation system, a reinforced concrete raft foundation provides load transfer and structural stability. This system consists of a 50 cm-thick raft slab and foundation beams with cross-sections measuring 90 × 230 cm, 60 × 230 cm, and 50 × 230 cm.

2.4. Field Investigation and Material Testing

To reduce uncertainties stemming from material degradation and construction variances, concrete testing and rebar scanning were performed concurrently with the post-earthquake structural reconnaissance. Concrete core samples were extracted from primary vertical and horizontal structural components across multiple stories to conduct compressive strength, carbonation, and chloride ion concentration tests, establishing baseline data for the nonlinear constitutive models. Additionally, rebar scanning was conducted to eliminate uncertainties related to construction placement deviations.

2.4.1. Rebar Layout Scanning

Non-destructive rebar scanning was conducted to verify the reinforcement configurations, rebar spacing, and concrete cover thickness of the beams and columns across multiple stories. The scanning program encompassed 51 beam and 54 column locations, totaling 105 inspected regions. The results demonstrated that 100 locations (approximately 95.3%) conformed to the original structural drawings; only 5 locations exhibited localized discrepancies, which were potentially attributable to measurement tolerances. Consequently, the reinforcement layouts specified in the design drawings were adopted as the analytical baseline for the numerical model.

2.4.2. Concrete Material Testing

Cylindrical concrete core samples were extracted from representative shear wall components and tested in accordance with regulatory standards. The testing program comprised 19 water-soluble chloride ion content tests, alongside 54 carbonation depth and compressive strength tests. Statistical analysis indicated that the mean in-situ concrete compressive strength exceeded the nominal design value. Regarding durability parameters, the mean carbonation depth from the 1st to the 9th story was 0 mm, with minor carbonation detected only at the 13th, 14th, and 15th stories. Furthermore, the chloride ion concentrations across all specimens were below 0.035 kg/m^3, well within the regulatory threshold limit of 0.15 kg/m^3. These findings verify that the concrete matrix had not undergone significant material degradation prior to the seismic event.

2.5. Observed Earthquake Damage

Post-earthquake field reconnaissance following the 3 April 2024 event documented severe structural damage to the exterior RC wall, as highlighted within the red box in Figure 8a. Widespread tile spalling and diagonal shear cracking were observed along the wall structure extending from the 2nd to 9th stories, demonstrating that this region was subjected to substantial lateral shear demands during the seismic excitation.

Interior damage inspection revealed a progressive decrease in structural severity from lower to upper stories. The most severe failure occurred on the second floor, characterized by localized concrete spalling measuring approximately 30 cm × 15 cm (Figure 9a). On the third floor, spalling of the concrete cover was observed, leaving the primary longitudinal reinforcement partially exposed (Figure 9b). Across the 4th to 6th stories, damage was predominantly manifested as shear cracking with widths of approximately 5 mm, accompanied by localized detachment of the surface tiles (Figure 9c–e). These observed damage patterns consistently reflect the concentration of high shear strain demands in the lower stories during the seismic event.

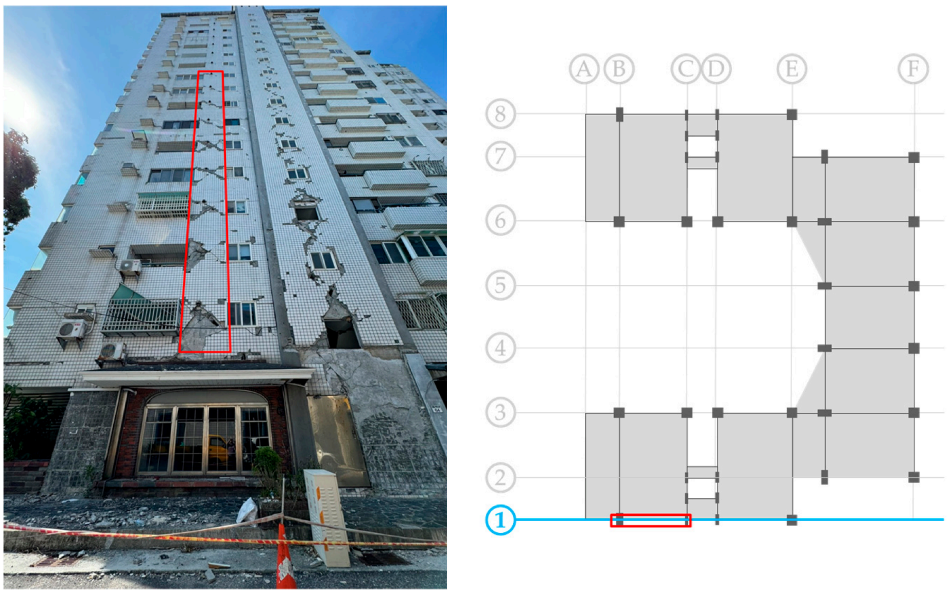

(**a**) (**b**)

Figure 8. Exterior field damage reconnaissance following the 3 April 2024 earthquake: (**a**) elevation view showing the damage condition of the exterior RC wall; (**b**) plan view illustrating the corresponding damage locations. (Numbers 1–8 and letters A–F indicate the transverse and longitudinal structural grid lines, respectively).

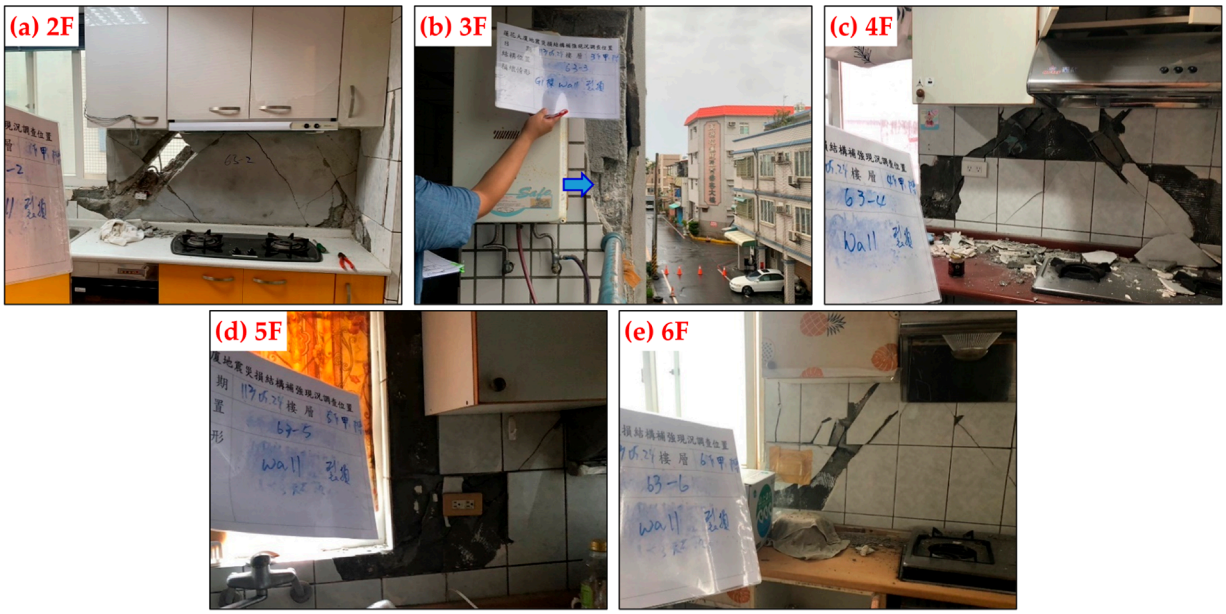

Figure 9. Interior damage observations across different story levels: (**a**) localized concrete spalling (approx. 30 cm × 15 cm) on the 2nd-floor wall; (**b**) concrete cover spalling with exposed primary longitudinal rebar on 3F; (**c**–**e**) tile spalling and shear cracking on 4F, 5F, and 6F, respectively.

Severe structural damage was similarly observed along the stairwell structural wall on the same side. Substantial tile spalling accompanied by diagonal shear cracking manifested around the upper and lower edges of various window openings (Figure 10a), representing a characteristic shear failure mode.

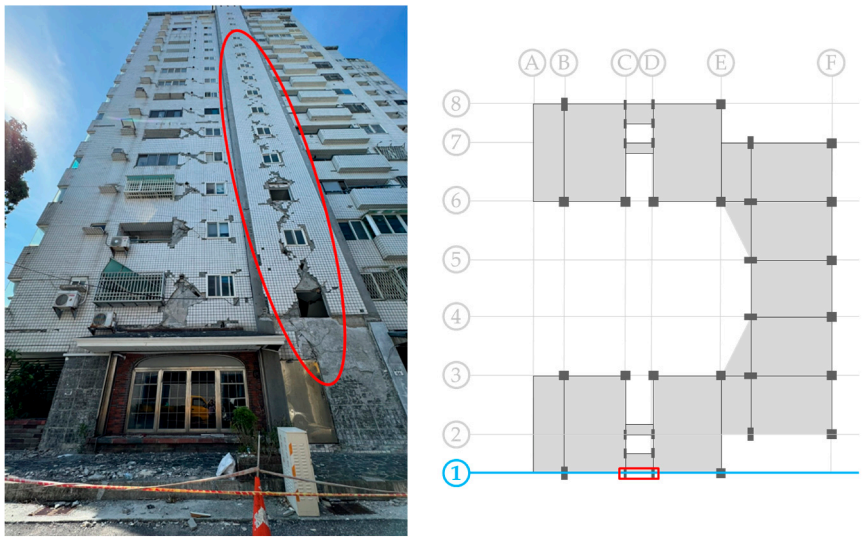

(**a**) (**b**)

Figure 10. Field damage reconnaissance of the stairwell wall along Frame 1: (**a**) exterior stairwell wall exhibiting tile spalling and diagonal shear cracking; (**b**) plan view illustrating the corresponding inspection location. (Numbers 1–8 and letters A–F indicate the transverse and longitudinal structural grid lines, respectively).

On the second floor, two major localized concrete spalling and crushing zones—measuring approximately 30 cm × 20 cm—were identified along the stairwell wall, exposing the underlying steel reinforcement and confirming that the component experienced severe nonlinear deformation (Figure 11b). Simultaneously, interior inspection revealed extensive spalling of the concrete cover, with the wall heavily traversed by a dense distribution of shear cracks exceeding 3 mm in width, reflecting significant structural degradation of the wall system (Figure 11a,c–f).



Figure 11. Interior damage observations of the stairwell wall across different story levels: (**a**,**d**–**f**) concrete cover spalling and shear cracking, with crack widths ranging from 3 mm to more than 5 mm; (**b**) localized concrete spalling and crushing (approximately 30 cm × 20 cm), with partially exposed reinforcement; (**c**) through-wall shear crack at the lower section.

Along Frame 2, post-earthquake reconnaissance photographs revealed relatively minor damage to the stairwell wall (Figure 12). In contrast, the structural wall on the first story suffered the most severe damage across the entire building. A prominent major diagonal shear crack—extending approximately 9 m from the upper left to the lower right—was clearly visible on the exterior, indicating a shear-dominated failure mechanism accompanied by extensive spalling of the concrete cover.

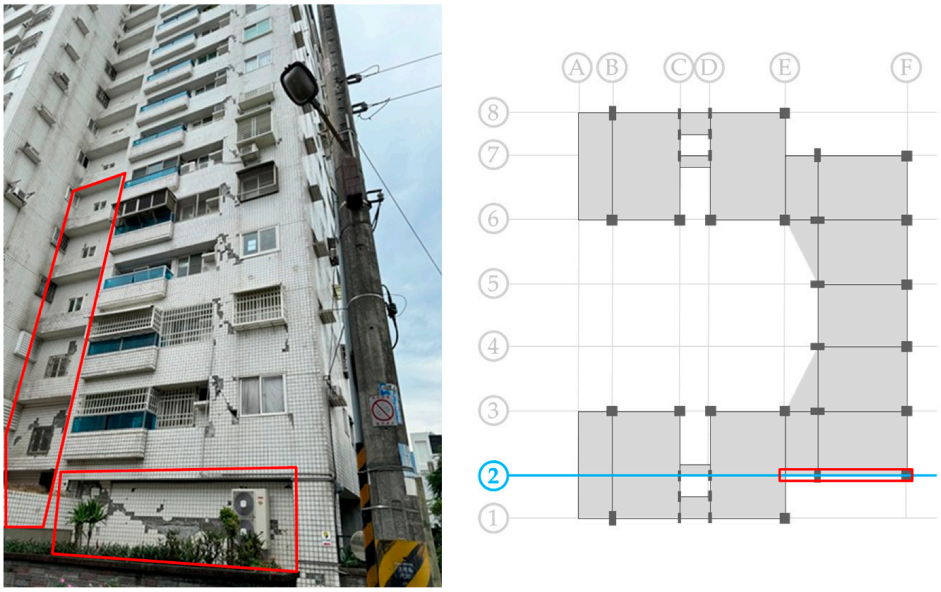

(**a**) (**b**)

Figure 12. Field damage reconnaissance of the stairwell wall along Frame 2: (**a**) elevation view showing damage locations on the exterior wall; (**b**) plan view illustrating the corresponding inspection location. (Numbers 1–8 and letters A–F indicate the transverse and longitudinal structural grid lines, respectively).

Interior inspection confirmed that this primary crack had developed into a through-wall fracture, with the affected through-crack zone spanning approximately 20 cm in width and reflecting substantial structural degradation (Figure 13).

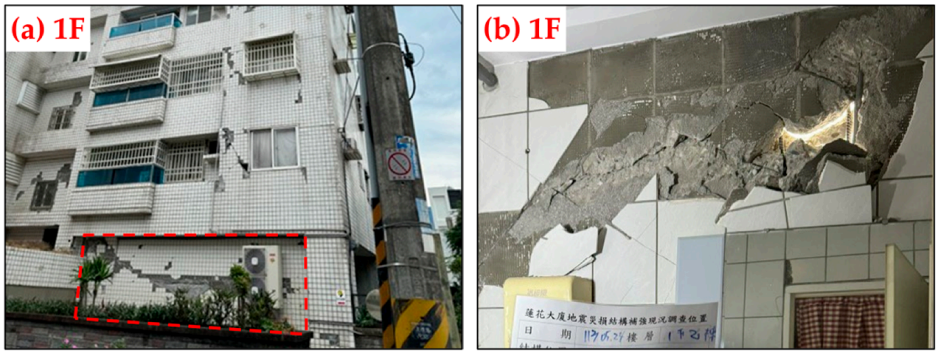

Figure 13. Post-earthquake inspection of the primary through-wall shear crack on the first-story structural wall: (**a**) exterior damage observation; (**b**) interior damage observation.

By comparison, the adjacent stairwell wall exhibited a dense distribution of minor cracking, with crack widths predominantly around 1 mm and local hairline cracks (Figure 14). On the 5th story and above, no visible cracking could be discerned from the interior inspection.



Figure 14. Minor cracking patterns on the stairwell walls: (**a**) concrete cover spalling with approximately 1 mm crack; (**b**) concrete cover spalling with approximately 1 mm crack; (**c**) hairline cracking; (**d**) hairline cracking. (The blue arrows indicate the specific crack locations, and the red dashed lines delineate the propagation paths of the cracks).

3. Methodology

This chapter delineates the numerical modeling framework and analytical methodologies implemented to simulate the nonlinear dynamic responses of the investigated structure. First, a three-dimensional finite element model of the 17-story plan-irregular RC building was constructed in ETABS, with boundary conditions defined based on the foundation type and site-specific conditions. Second, the calibration and configuration of the Rayleigh damping parameters are explained to ensure the numerical soundness of the dynamic solution. Subsequently, the mechanics-based nonlinear constitutive relationships for the plastic hinges of the beams, columns, and shear walls—derived via the SERCB platform—are detailed. Next, the selection criteria and standardization methodology for the input ground motions are described. Finally, a displacement-based ductility demand index (*D* index) is introduced, followed by the formulation of a multi-dimensional validation strategy to objectively evaluate the reliability of the proposed numerical framework.

3.1. Finite Element Model Construction and Boundary Conditions

A three-dimensional finite element model of the investigated structure was constructed (Figure 15) to simulate its nonlinear dynamic responses under the 2024 Hualien earthquake. Based on the original design drawings, the structure is an RC building consisting of 17 stories above ground and 1 basement level, with a total height of 49.6 m. The cross-sectional dimensions, reinforcement configurations, and spatial distributions of the beams, columns, and shear walls were implemented in accordance with the design drawings to ensure that the load-resisting and load-transfer mechanisms of the global structural system were accurately reflected.

Regarding the material properties, although the concrete core testing results surpassed the specified design values, the nominal design strengths were adopted in the numerical

model to maintain a conservative approach for the seismic evaluation. The material parameters are specified as follows: the compressive strength of concrete (f'_c) is 21 MPa; the yield strength (f_y) of rebars smaller than or equal to #5 is 280 MPa (SD280), whereas that of longitudinal reinforcements larger than or equal to #6 is 420 MPa (SD420). Additionally, the compressive strengths of the red bricks and cement mortar for the infill masonry walls are defined as 15 MPa and 10 MPa, respectively.

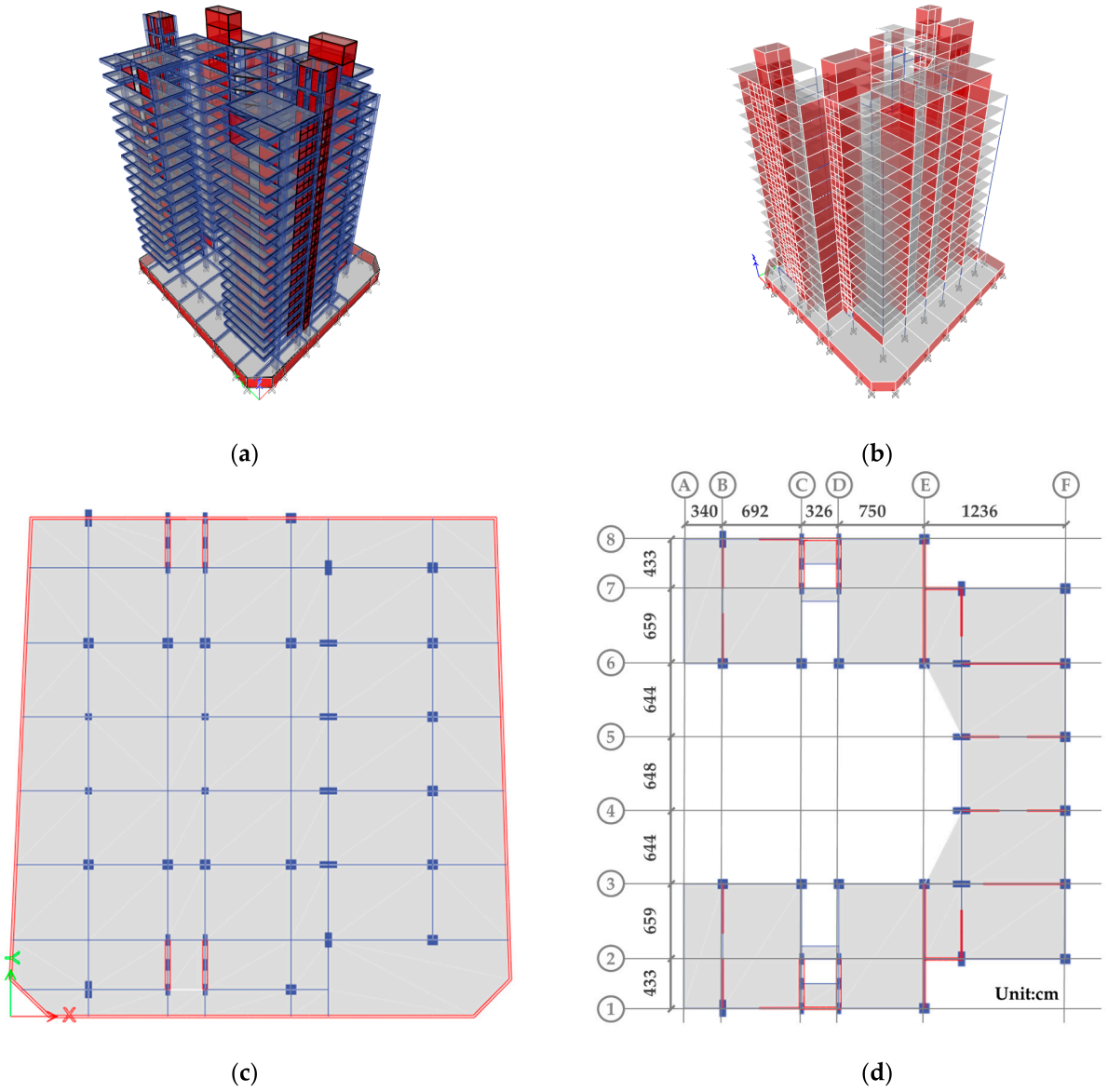

Figure 15. ETABS structural numerical model: (**a**) 3D model (front perspective); (**b**) 3D model (rear perspective); (**c**) base plan view; (**d**) typical floor plan view. (Numbers 1–8 and letters A–F indicate the transverse and longitudinal structural grid lines, respectively).

A rigid diaphragm assumption was applied to the floor system to reflect the transfer of lateral inertial forces across each story level. Furthermore, a fixed-base boundary condition was implemented at the model base, thereby neglecting soil–structure interaction (SSI) considerations. This assumption was adopted on the basis that the structure is supported by a raft foundation resting upon a dense gravelly sand stratum, characterized by Standard Penetration Test blow counts reaching N = 100. Based on depth-resolved SPT-N measurements, the average shear-wave velocity within the upper 30 m (V_{s30}) was evaluated as 381.4 m/s, corresponding to a Class I site condition according to the Taiwan seismic design

code. Given the high structural stiffness provided by the combined foundation–stratum system, the potential influence of SSI is secondary relative to the overall nonlinear dynamic response of the superstructure, justifying its exclusion in this investigation.

3.2. Rayleigh Damping Calibration and Numerical Solution Control

In the developed finite element model, NDTHA was executed utilizing the direct integration method. To simulate the energy dissipation behavior of the structure under seismic excitation, a Rayleigh damping model was implemented, wherein the mass- and stiffness-proportional damping coefficients were calibrated by specifying target damping ratios at two critical control periods.

The first control point was designated at the primary dominant mode of the structure (Mode 1, T = 1.421 s), and the second was selected at a higher-order mode (Mode 16, T = 0.128 s). The nominal structural damping ratio for both control points was specified as 5%, consistent with conventional reinforced concrete systems. Selecting these two control points ensures that the dynamic responses of the dominant modes are accurately captured while maintaining the damping ratios within a reasonable threshold across the intermediate frequency spectrum. This configuration prevents higher-order modes from being subjected to artificial overdamping, which would otherwise suppress high-frequency dynamic responses. Furthermore, this approach effectively mitigates high-frequency numerical noise, thereby enhancing convergence and numerical stability during the nonlinear time-history solution process.

3.3. SERCB-Based Plastic Hinge Modeling for RC Members

A lumped plasticity model was implemented to characterize the post-yield behavior of the primary structural elements under seismic excitation. Nonlinear plastic hinges were assigned to both ends of the beams and columns, while nonlinear shear hinges were assigned to the shear walls. The elastoplastic properties of these hinges were derived using the SERCB, which is approved by the National Land Management Agency (NLMA) for the seismic performance evaluation of RC structures. The SERCB performs nonlinear analysis to generate moment–curvature (M–φ) and moment–rotation (M–θ) relationships, which are subsequently transformed into element-level elastoplastic backbone curves (Figure 16). This analytical approach explicitly accounts for material nonlinearity, rebar yielding, and concrete crushing within the plastic hinge zone [27].

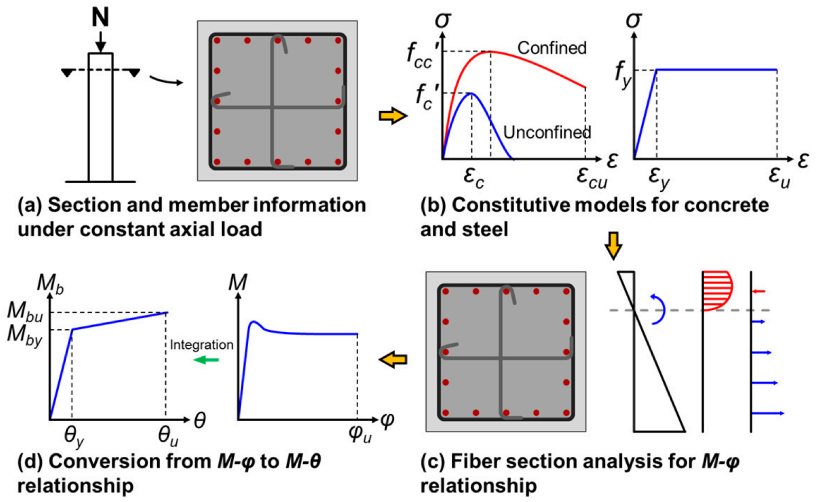

Figure 16. Analytical flowchart of the section-to-component plastic hinge properties derived via SERCB [27].

Lai and Sung [28] established an analytical methodology to evaluate the nonlinear behavior of low-rise RC shear walls. Requiring wall dimensions, material properties, and reinforcement details as inputs, the workflow directly adopts the diagonal angle of the wall as the principal stress direction. The computation employs an iterative procedure: the applied shear force is incrementally increased while the principal compressive and tensile strains are simultaneously adjusted. Accounting for concrete softening effects, the biaxial compressive and tensile stresses are determined. Based on strain compatibility, the strains are transformed into the reinforcement directions to calculate the transverse and longitudinal steel stresses. The total shear capacity is obtained by summing the concrete and reinforcement contributions; once convergence between the calculated capacity and the target shear force is satisfied, the top horizontal displacement of the wall at that specific stage is derived. This iterative cycle continues until the principal compressive strain of the concrete reaches its ultimate limit, thereby establishing the horizontal shear force–displacement relationship of the wall.

Although prior implementations were restricted by contemporary numerical software limitations and necessitated the transformation of this relationship into the axial force–displacement curves of equivalent diagonal strut elements via geometric projection, modern commercial platforms such as ETABS permit the direct simulation of shear walls utilizing shell elements. Consequently, instead of executing the axial transformation proposed in the original literature, this relationship was directly implemented as a nonlinear shear hinge formulation within the shell elements, with the resulting characteristic mechanical points defining the plastic hinge properties of the shear wall.

To simulate cyclic degradation and energy dissipation under cyclic loading, the Takeda hysteresis model was applied to define the hysteretic behavior of these nonlinear hinges, incorporating stiffness degradation rules for both the unloading and reloading paths. The control points of the SERCB plastic hinge are illustrated in Figure 17, where Points B, C, D, and E denote the cracking, yielding, peak strength, and ultimate deformation limits of the element, respectively.

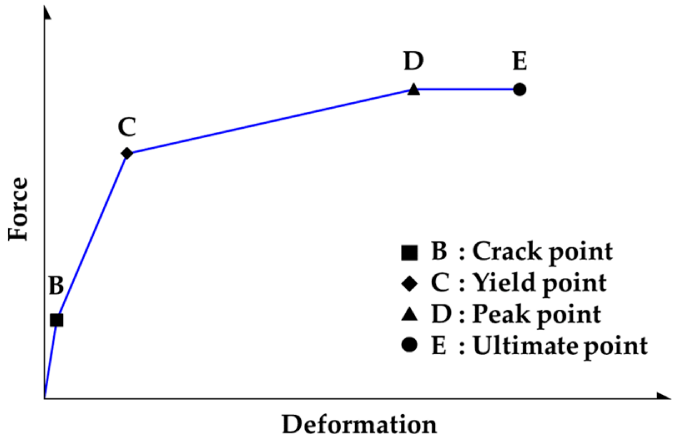

Figure 17. Definitive definitions of key performance thresholds (Points B to E) on the SERCB plastic hinge backbone curve [27].

To evaluate the nonlinear response of the target building, the mechanics-based SERCB framework was adopted, and its nonlinear member properties were compared with the generalized hinge formulations available in FEMA/ASCE 41. FEMA/ASCE 41 provides widely used acceptance criteria and generalized nonlinear component parameters for seismic evaluation of existing buildings, offering a practical and standardized approach for nonlinear modeling. In contrast, SERCB provides RC member-specific procedures for defining nonlinear properties based on the specified material properties, member dimensions,

and reinforcement details, including section moment–curvature, member moment–rotation, and shear behavior. This feature is particularly relevant to the present case study because detailed information on the structural sections, reinforcement, and material properties of the investigated building was available from design documents and post-earthquake investigations. Therefore, rather than assuming that SERCB is universally superior to FEMA/ASCE 41, the present study adopts SERCB because its member-specific formulation provides a suitable basis for representing the actual RC member characteristics of the investigated building. The resulting nonlinear properties were subsequently incorporated into ETABS for nonlinear dynamic time-history analysis and evaluated against the observed post-earthquake damage.

3.4. Selection of Ground Motion Records

To replicate the field-observed seismic damage modes, the ground motion records captured during the 2024 Hualien earthquake were adopted as the seismic input for the nonlinear time-history analysis. Strong-motion records from the HWA019 station, located within Hualien City, were selected. The spatial distance between this recording station and the target building is approximately 2.25 km (Figure 18). Given this geographical proximity, the two sites share similar local soil conditions, wave propagation paths, and site-amplification effects. Consequently, the acceleration time histories recorded at the HWA019 station represent the ground motion characteristics experienced by the target structure.

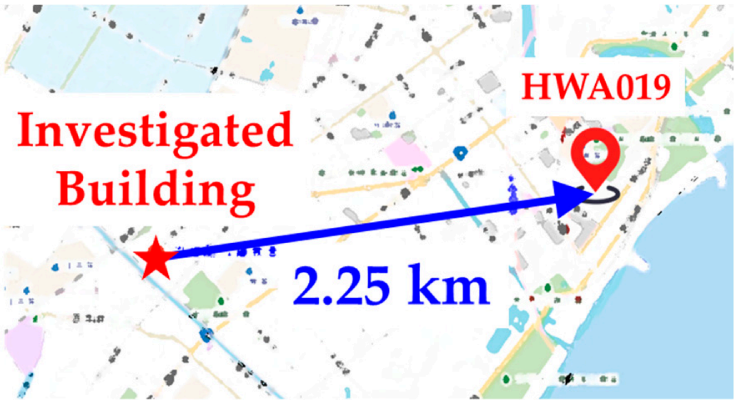

Figure 18. Spatial proximity and relative locations of the HWA019 strong-motion station and the investigated building, adapted from geospatial data provided by GSMMA, MOEA [25], and station information from the Central Weather Administration (CWA) [2].

To evaluate potential site amplification effects, the geological condition of the HWA019 station was assessed based on CWA records. The station has an estimated V_{s30} of approximately 503 m/s, which belongs to a Class I site (V_{s30} > 270 m/s), consistent with the target building site. Considering the shared stiff soil conditions and the short distance (2.25 km) between the recording station and the target structure, the differences in site amplification are negligible within engineering tolerances, justifying the direct use of the uncorrected HWA019 records as the input motion.

Figure 19 displays the triaxial peak ground accelerations (PGAs) extracted from the HWA019 station records: 457.96 gal in the north–south (NS) direction, 255.99 gal in the east–west (EW) direction, and 208.53 gal in the vertical (V) direction. The raw signals underwent mean removal, bandpass filtering with specific cutoff frequencies, and baseline correction using polynomial fitting. Notably, the NS-direction PGA reached approximately 0.46 g, indicating that this axis served as the primary energy input channel and dominated the overall inertial response. To represent the authentic seismic demand of the 3 April 2024 Hualien earthquake, no amplitude scaling was applied to the acceleration time histories.

For the NDTHA configuration, the triaxial acceleration time histories were applied simultaneously in ETABS to simulate the three-dimensional elastoplastic dynamic response of the global structural system. This synchronized triaxial excitation enabled the numerical model to capture multidirectional coupling effects, including the interaction between translational and torsional responses.

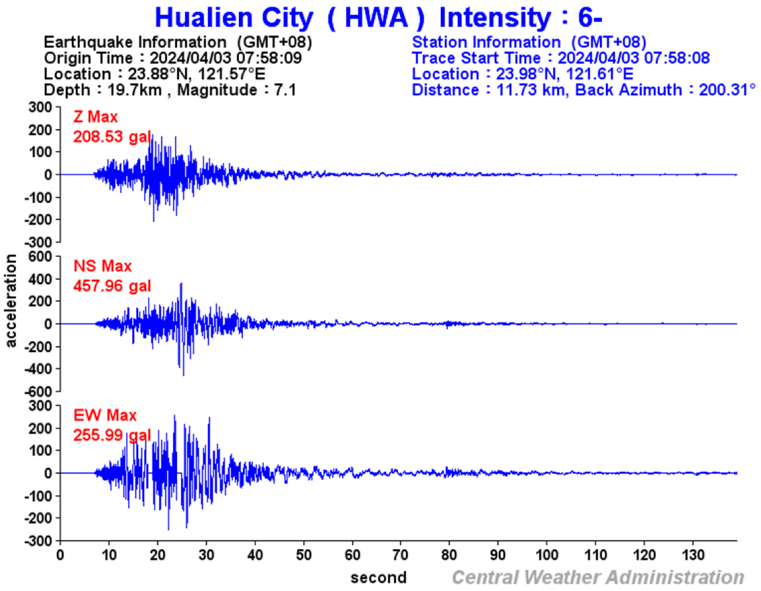

Figure 19. Triaxial acceleration time histories recorded at the HWA019 station during the 2024 Hualien earthquake, sourced from CWA ground motion records [2].

As illustrated in Figure 20, the 5% damped acceleration response spectrum of the recorded HWA019 ground motion is evaluated and compared directly against the code-defined Design Basis Earthquake (DBE) and Maximum Considered Earthquake (MCE) design spectra. The first three fundamental vibration periods of the target building—T_1 = 1.421 s, T_2 = 1.277 s, and T_3 = 1.101 s—are explicitly indicated with vertical dashed lines.

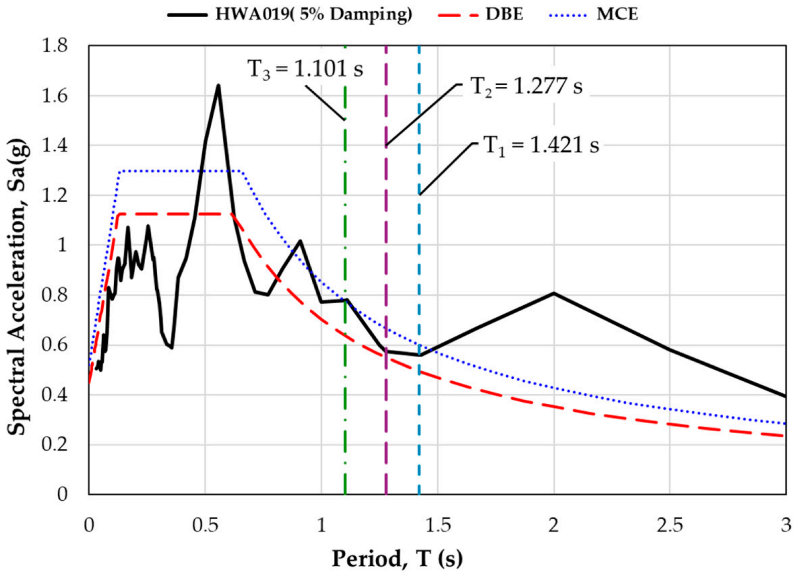

Figure 20. Figure showing 5% damped acceleration response spectrum of the HWA019 ground motion record compared with the code-specified DBE and MCE design spectra, with the building's first three natural vibration periods (T_1 = 1.421 s, T_2 = 1.277 s, and T_3 = 1.101 s) indicated.

Within the predominant structural period band (T = 1.101 s to 1.421 s), the spectral acceleration demands of the HWA019 motion generally lie between the DBE and MCE levels, closely aligning with the MCE demand curve near T_3. This demonstrates that the ground motion imposed significant inelastic energy demands on the structure, providing a clear spectral justification for the severe damage observed in the lower-story shear walls.

3.5. Displacement-Oriented Ductility Index and Damage Mapping

In this study, the seismic damage states of RC shear walls are classified into five levels (I to V). As tabulated in Table 4, the thresholds for each damage state are established based on physical damage features observed during field reconnaissance, including crack propagation patterns, maximum crack widths, the extent of reinforcement exposure, and the structural integrity of the boundary elements.

Table 4. Classification of Seismic Damage States.

Damage State (Level)	Schematic	Cracking Patterns and Widths	Reinforcement & Boundary Column Status
Slight (I)	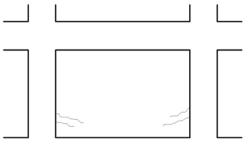	Minor horizontal cracks; width $w < 0.3$ mm.	No reinforcement exposure or concrete spalling.
Moderate (II)		Propagated horizontal cracks extending to boundary columns; width $0.3 < w < 1$ mm.	Minor cracking in boundary elements; no structural degradation.
Significant (III)	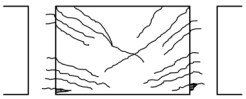	Prominent diagonal (shear) cracks initiated in the wall web.	Internal reinforcement remains unexposed.
Severe (IV)	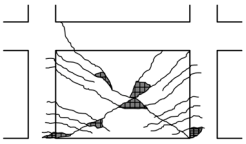	Proliferation of extensive and intersecting diagonal shear cracks.	Clear exposure of longitudinal bars; spalling of boundary column cover.
Collapse (V)	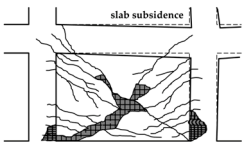	Wide, severe diagonal cracks propagating throughout the web.	Tensile fracture or buckling of primary bars; severe concrete crushing of boundary elements; slab subsidence.

Note: Redrawn based on the criteria specified in the Emergency Assessment Form for Hazardous Buildings after Disasters [29].

During the initial stage of lateral loading, the structure remains intact with crack widths within 0.3 mm, which is defined as Slight (I). As seismic demand increases, horizontal cracks with widths ranging from 0.3 to 1 mm develop on the wall surface, designating the damage state as Moderate (II). Upon further deformation, these horizontal cracks propagate toward the boundary elements and transition into diagonal shear cracks with widths exceeding 1 mm while the reinforcement remains unexposed, classifying the state as Significant (III). Beyond this stage, the damage progresses to Severe (IV), characterized by intersecting diagonal shear cracks accompanied by concrete cover spalling and rebar exposure. Ultimately, the component reaches Collapse (V), where the diagonal cracks widen and penetrate the wall web; the core concrete undergoes crushing and disintegration, while the primary longitudinal bars exhibit tensile fracture or buckling. This failure of the

boundary elements leads to structural slab subsidence, indicating that the shear wall is on the verge of complete failure.

To establish a quantitative correlation between the NDTHA results and the corresponding structural degradation, thereby assessing the evolution of plastic hinge ductility under seismic excitation, a displacement-based normalized ductility development index (D) was adopted in this study [30,31]. This index evaluates the maximum structural displacement demand relative to the interval between the yielding and ultimate displacements, thereby characterizing the elastoplastic response of structural elements from the elastic regime to progressive damage development. It should be noted that cumulative damage and low-cycle fatigue effects induced by repeated cyclic loading are not explicitly quantified in the definition of the D index; rather, the index serves as a deformation-based indicator for characterizing damage states. Nevertheless, cyclic stiffness degradation and hysteretic energy dissipation are incorporated into the nonlinear analysis through the Takeda hysteretic model. The index is mathematically formulated as follows:

$$D = (\Delta - \Delta_y)/(\Delta_u - \Delta_y) \quad (1)$$

where Δ is the maximum response displacement captured during the analysis history; Δ_y is the yield displacement, signifying the onset of nonlinear structural behavior and the initiation of ductility development; and Δ_u is the ultimate displacement, corresponding to strength degradation or complete loss of load-carrying capacity.

This ductility development index carries the following physical interpretation: for $\Delta < \Delta_y$, $D = 0$, indicating that the element remains within the elastic regime where ductility has not yet mobilized; for $\Delta = \Delta_u$, $D = 1$, representing structural failure where the available ductility capacity is fully exhausted. Consequently, this index serves as a quantified parameter for damage evaluation and can be extended to classify structural performance levels, such as slight, moderate, severe, and collapse prevention.

Upon establishing the performance thresholds of the backbone curve and the calculation criteria for ductility consumption, the quantitative thresholds for the five seismic damage states—Slight (I), Moderate (II), Significant (III), Severe (IV), and Collapse (V)—were defined (Figure 21). Between the cracking and yield points, the element operates within the elastic or micro-cracking regime, where the formation of hairline cracks does not compromise structural performance, classifying the state as Slight (I). Once the deformation surpasses the yield point with the ductility development index falling within $0 < D \leq 0.2$, the structure transitions into the nonlinear regime; crack propagation accelerates, crack widths reach 0.3–1 mm, and the element sustains repairable damage, designating the state as Moderate (II).

When the ductility consumption reaches the 20–50% range ($0.2 < D \leq 0.5$), diagonal shear cracks emerge across the wall web and the concrete cover initiates localized spalling, yet the primary longitudinal bars remain unexposed, categorizing the damage as Significant (III). As the ductility mobilization advances to the 50–80% range ($0.5 < D \leq 0.8$), the seismic capacity of the element approaches saturation, characterized by concrete cover delamination and direct exposure of the internal reinforcement without fracture or buckling, representing Severe (IV). Ultimately, when the ductility consumption exceeds 80% ($0.8 < D \leq 1.0$), crushing and disintegration of the core concrete occur, and the primary longitudinal reinforcements undergo tensile fracture or buckling, indicating that the element is on the verge of complete failure, defined as Collapse (V).

This quantitative relationship linking plastic hinge evolution to structural damage levels provides a basis for post-earthquake structural vulnerability assessment and engineering decision-making.

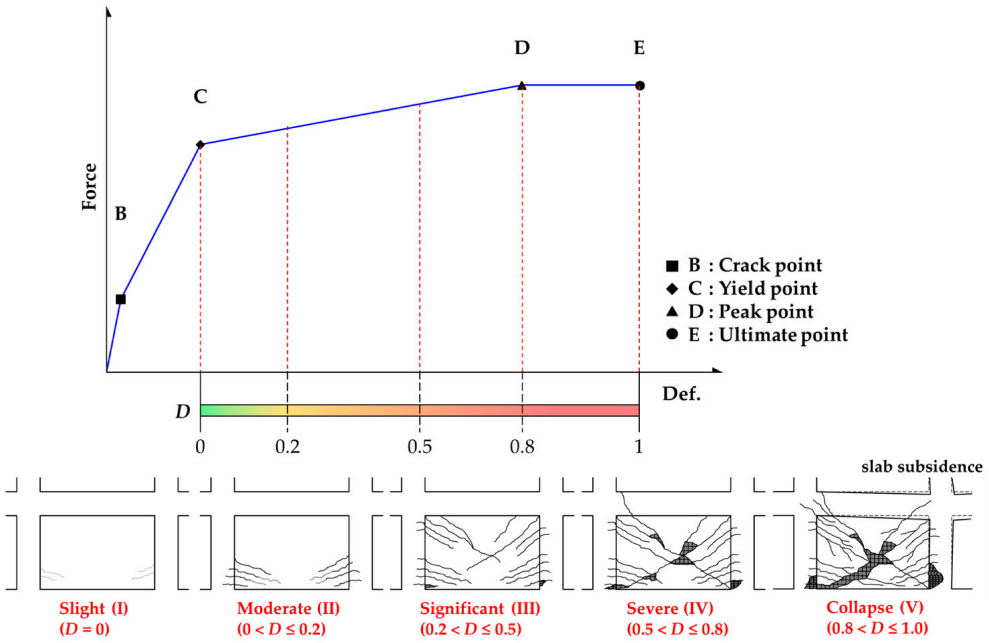

Figure 21. Quantitative mapping relationships between the SERCB plastic hinge backbone curve, the ductility development index *D*, and corresponding seismic damage states.

3.6. Validation Strategy

To verify the accuracy of the nonlinear numerical model and analytical results, the simulation outputs were compared and cross-referenced with the field-observed structural damage from the 2024 Hualien earthquake. First, the spatial distribution of structural damage induced by eccentric torsional behavior within the plan-irregular layout was evaluated. This cross-check aims to assess the capability of the numerical model to capture localized damage boundaries at the outermost perimeter frames.

Second, regarding local component-level damage, a quantitative classification strategy was implemented based on component ductility indices and critical plastic hinge characteristic points. This strategy transforms the maximum deformation responses from the nonlinear direct integration time-history analysis into discrete damage states. By extracting the maximum transient deformations of individual elements from the NDTHA, their corresponding *D* indices were computed. Finally, the analytically derived damage grades were cross-referenced with field-observed physical damage—such as localized cracking, concrete spalling, and shear cracks—to quantitatively validate the simulated seismic performance.

Furthermore, a cross-verification mechanism was implemented targeting representative components across varying damage severities—including undamaged, slight, moderate, and severe states—to analyze their local responses and nonlinear hysteretic behavior. Because field reconnaissance exclusively captures post-earthquake residual states, this study utilizes NDTHA to extract the analytical nonlinear hysteretic pathways, maximum deformation points, and cumulative plastic dissipation energy experienced by these typical components throughout the seismic timeline.

By cross-referencing the hysteretic trajectories—where undamaged elements remain within the linear-elastic regime, slightly to moderately damaged elements surpass the cracking (Point B) or yielding (Point C) thresholds, and severely damaged elements approach their peak strength (Point D) or ultimate deformation limits (Point E)—the analytically derived time-dependent mechanics are physically mapped onto the observed field failure modes. This explicit linking of transient dynamic mechanisms to physical structural damage enhances the scientific validity of the quantitative verification.

4. Results

This chapter presents the numerical simulation results to evaluate the dynamic behavior, torsional irregularity, and seismic damage of the structure. Section 4.1 details the modal analysis, establishing the baseline for natural frequencies and mode shapes. Building upon this, Section 4.2 conducts the eccentricity analysis to quantify the offsets between the center of mass (CM) and center of rigidity (CR). Finally, Section 4.3 correlates the simulated and actual damage to validate the numerical model, specifically mapping plastic hinge behaviors and *D* index correlations against field-observed damage patterns. Together, these findings successfully reveal the critical mechanisms governing the structural failure and seismic damage.

4.1. Modal Analysis

As shown in Table 5, the modal analysis results indicate that the dynamic behavior in the *x*-direction is primarily governed by the second mode (*x*-directional translation), with an effective mass participation factor of 66%. In contrast, the dynamic response in the *y*-direction involves the first and third modes, which account for participation ratios of approximately 32% and 31%, respectively. Observations of the first and third mode shapes reveal that both exhibit torsional components, reflecting the plan irregularity and translational–torsional coupling effects within the building configuration. The characteristics of the first three mode shapes are illustrated in Figure 22.

Table 5. Modal periods and participating mass ratios.

Mode	Period Sec	UX	UY	ΣUX	ΣUY	RX	RY	RZ	ΣRX	ΣRY	ΣRZ
1	1.421	0.01%	32.55%	0.01%	32.55%	10.93%	0.00%	31.40%	10.93%	0.00%	31.40%
2	1.277	66.20%	0.43%	66.21%	32.98%	0.14%	25.90%	0.29%	11.07%	25.91%	31.69%
3	1.101	0.72%	31.19%	66.94%	64.17%	9.98%	0.31%	35.54%	21.05%	26.21%	67.23%
4	0.366	1.48%	2.53%	68.42%	66.70%	0.61%	2.58%	10.05%	21.66%	28.80%	77.28%
5	0.349	14.02%	0.61%	82.44%	67.30%	0.26%	23.34%	0.98%	21.92%	52.13%	78.26%
6	0.313	0.06%	0.02%	82.50%	67.33%	0.39%	0.04%	0.18%	22.31%	52.18%	78.44%
7	0.309	0.35%	0.00%	82.85%	67.33%	0.07%	0.32%	0.06%	22.38%	52.49%	78.50%
8	0.295	0.06%	12.05%	82.92%	79.38%	14.07%	0.11%	1.58%	36.45%	52.60%	80.08%
9	0.291	0.03%	1.81%	82.95%	81.19%	0.38%	0.03%	0.91%	36.82%	52.63%	80.99%
10	0.275	0.17%	0.01%	83.11%	81.20%	0.02%	0.23%	0.00%	36.85%	52.86%	80.99%

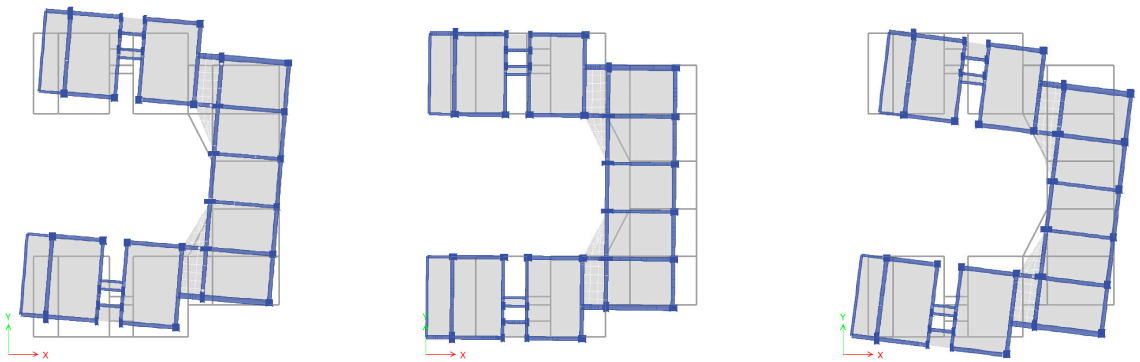

(**a**) (**b**) (**c**)

Figure 22. Structural mode shapes of the first three vibration modes determined from the numerical model: (**a**) Mode 1 (Translation Y and Torsion Z), (**b**) Mode 2 (Translation X), and (**c**) Mode 3 (Translation Y and Torsion Z).

4.2. Eccentricity Analysis

To evaluate the structural irregularity and potential torsional vulnerability, the eccentricity ratios along the *x*- and *y*-directions from the 1st to the 17th stories were computed. Table 6 lists the specific eccentricity data for these floor levels. The eccentricity ratios reveal a pronounced directional variation. The *x*-direction exhibits larger eccentricities than the *y*-direction, indicating a greater separation between the centers of mass and rigidity along this axis. This directional asymmetry suggests that the structural configuration is highly susceptible to torsional effects, particularly under seismic excitation interacting with the larger *x*-directional eccentricity. Consistent with this analysis, the subsequent nonlinear dynamic analyses show greater damage concentration in the exterior frames aligned with the *x*-direction, validating the influence of plan irregularity on the observed damage distribution.

Table 6. Eccentricity ratios from the 1st to the 17th stories.

Story	X-Direction Eccentricity Ratio (%)	Y-Direction Eccentricity Ratio (%)
17F	16.62	0.71
16F	16.08	0.77
15F	14.77	0.83
14F	13.67	0.91
13F	12.70	0.99
12F	11.77	1.07
11F	10.83	1.16
10F	9.84	1.25
9F	8.79	1.33
8F	7.62	1.41
7F	6.31	1.49
6F	4.81	1.56
5F	3.05	1.60
4F	0.90	1.60
3F	1.72	1.51
2F	4.98	1.27
1F	7.96	0.67

4.3. Correlation Between Simulation and Actual Damage

Based on the analysis results, Frame 1 and Frame 2 experienced the most severe plastic hinge development. Because these two frames are located at the outermost boundaries of the structure along the *x*-direction, they represent the regions most sensitive to intense torsional effects, where the outermost perimeter sustains the maximum additional deformation during twisting. This susceptibility provides a clear mechanical rationale for why these specific frames exhibited the most significant nonlinear failure during the 2024 Hualien earthquake, thereby justifying their selection as the priority targets for field reconnaissance and numerical validation.

Utilizing the NDTHA predictions, a cross-comparison was performed between the critical substructures (Frame 1 and Frame 2) and the field reconnaissance records. According to the simulation results extracted from ETABS (Figure 23), the wall shear hinges within multiple zones of the Frame 1 stairwell walls surpassed the cracking threshold and exceeded the primary reinforcement yielding point (denoted as Point C on the backbone curve). In contrast, several structural shear wall elements in Frame 2 exhibited wall shear hinge mobilization bounded tightly within the reinforcement yielding point (Point C), corresponding to a damage state classified between Slight (I) and Moderate (II).

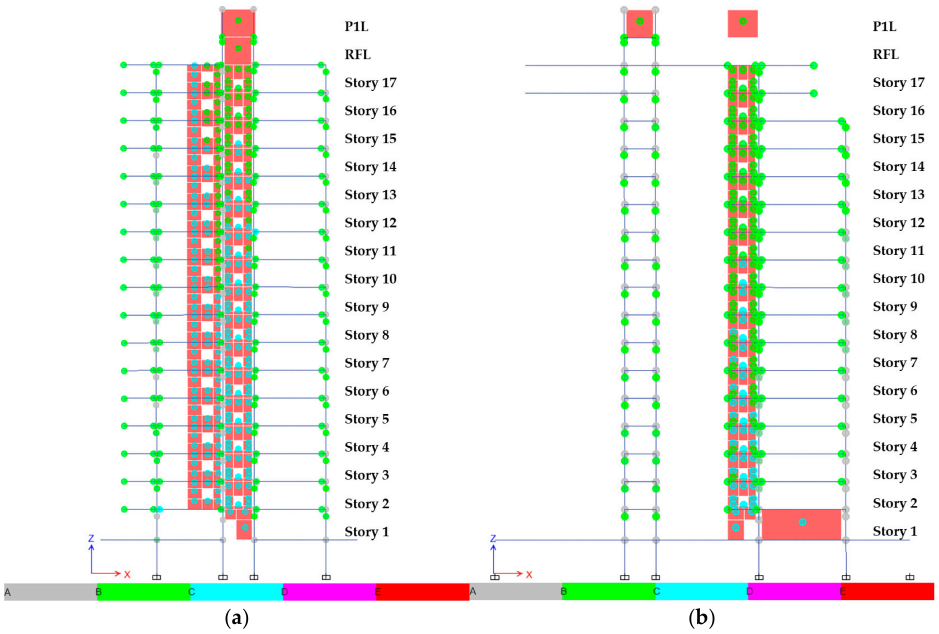

Figure 23. Nonlinear structural response profiles derived from NDTHA: (**a**) plastic hinge propagation in Frame 1 walls; (**b**) plastic hinge propagation in Frame 2 walls.

To correlate the simulated damage indices with the physical failure modes captured on-site—encompassing diagonal shear cracking, concrete cover delamination, and rebar exposure—an element numbering system was designated for the target structural components (Figure 24). Taking the designation "F1-2a" as an example, the prefix "F1" denotes Frame 1, the numeral "2" signifies the second-floor level, and the trailing lowercase letters ("a" and "b") distinguish individual wall panels within the same planar frame. This nomenclature facilitates the integration of local nonlinear numerical responses with the observed physical damage, thereby validating the estimated seismic performance against field observations.

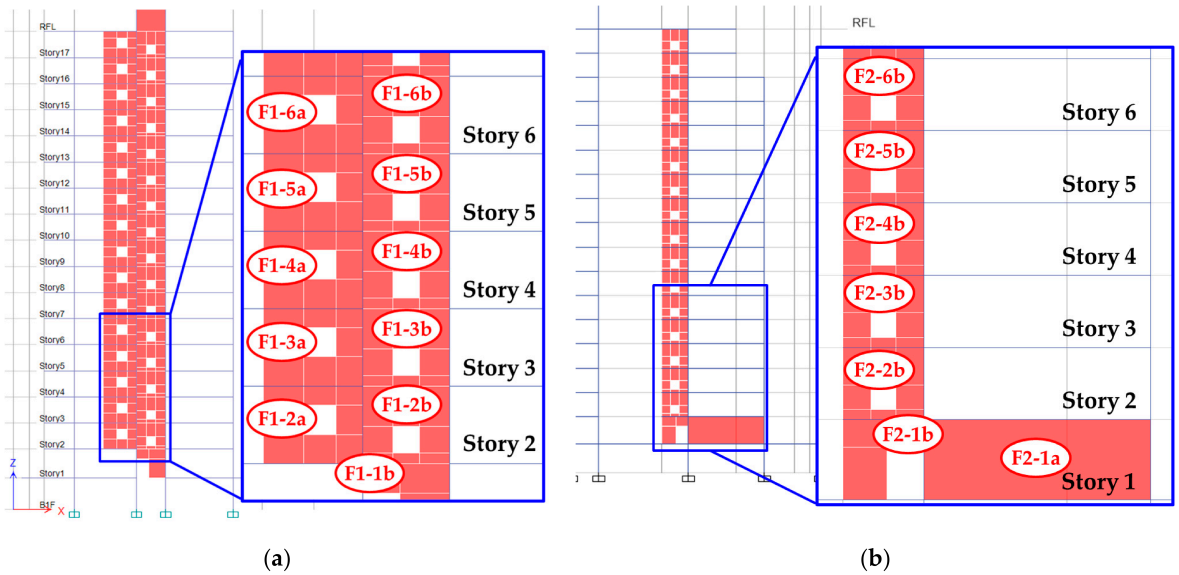

Figure 24. Schematic layout of the component identification numbering system for damage cross-verification: (**a**) kitchen and stairwell walls in Frame 1; (**b**) ground-floor walls and stairwell walls in Frame 2.

Table 7 summarizes the NDTHA analytical results and their direct correlation with post-earthquake field damage features for Frame 1 shear wall components under HWA019

excitation. The analytical outputs delineate key response parameters—including peak shear forces ($|V_{max}|$), maximum displacements ($|\Delta_{max}|$), ductility development indices (D), and simulated damage states (Simulated DS)—side-by-side with physical damage indicators recorded during reconnaissance.

Table 7. Comparison between analytical simulation results and field-observed damage states for Frame 1 wall components under HWA019 excitation.

Item	Analytical Simulation Results				Observed Field Damage Features				Correlation
	$\lvert V_{max} \rvert$ (kN)	$\lvert \Delta_{max} \rvert$ (mm)	D	Simulated DS	Crack Width (mm)	Cover Spalling	Rebar Exposure	Through-Wall Cracks	Observed DS	
F1-2a	281	8.74	0.229	III	>5	●	●	●	IV	Minor Dev.
F1-3a	282	8.98	0.238	III	>5	◑	○	-	III	Matched
F1-4a	283	9.1	0.243	III	>5	○	-	-	III	Matched
F1-5a	283	9.17	0.246	III	5	○	-	-	III	Matched
F1-6a	283	9.18	0.246	III	3–5	○	-	-	III	Matched
F1-1b	382	9.28	0.170	II	>5	◑	-	-	III	Minor Dev.
F1-2b	353	15	0.335	III	>5	●	●	●	IV	Minor Dev.
F1-3b	357	16.26	0.370	III	>5	●	◑	○	IV	Minor Dev.
F1-4b	360	17.01	0.391	III	5	◑	-	-	III	Matched
F1-5b	362	17.61	0.408	III	5	◑	-	-	III	Matched
F1-6b	363	17.95	0.418	III	3–5	◑	-	-	III	Matched

Note: Severity level of observed damage features: - = None; ○ = Slight; ◑ = Moderate; ● = Severe.

For the a-series elements (F1-2a to F1-6a), the analytical D indices range between 0.229 and 0.246, categorizing all simulated damage states as Significant (DS III). This indicates that these boundary members yielded and entered an elastoplastic state without experiencing complete structural collapse. Physically, a progressive decrease in observed crack widths (from >5 mm down to 3–5 mm) is recorded with ascending story level. Notably, F1-2a exhibited severe cover spalling, rebar exposure, and through-wall cracking, placing its field-assessed damage at DS IV (Minor Deviation), whereas elements F1-3a to F1-6a demonstrated an exact match (Matched) with the simulated DS III status.

Conversely, the b-series walls exhibit pronounced spatial variation in their lateral deformation demands. At the ground level, element F1-1b yields a D index of 0.170 (Simulated DS II), while ascending stories demonstrate a steady escalation in ductility demand, reaching D = 0.418 at the sixth story (F1-6b). This upward trend confirms that lateral displacement demands concentrate heavily within the lower-to-middle levels (Stories 2–6). Across the entire 18 evaluated wall components in Frame 1, 63.6% (7/11) achieved an exact match between the simulated and observed damage states, with all remaining discrepancies bounded within a single damage class margin (Minor Deviation). The hysteretic loops of critical elements and their spatial correlation with observed failure modes are further detailed in Figure 25.

Collectively, the D indices of Frame 1 shear walls predominantly span 0.2 to 0.4, verifying that these members actively engaged ductile hysteretic energy dissipation. The high quantitative correlation between numerical predictions and reconnaissance topology confirms that, within torsionally irregular structural systems, boundary frames are particularly vulnerable to localized deformation concentrations, thereby accelerating dynamic damage accumulation under triaxial seismic shaking.

Table 8 presents a comparative summary of the NDTHA predictions and field-observed damage features for the shear wall elements in Frame 2 under HWA019 excitation. The numerical results highlight that the ground-floor shear wall F2-1a developed a peak ductility index D of 0.546, corresponding to a simulated damage state of Severe (DS IV). This element experienced the most severe structural degradation within the Frame 2 model, which was strongly corroborated by post-earthquake reconnaissance data. Field evidence confirmed extensive physical damage, including severe cover spalling, longitudi-

nal rebar exposure, and a penetrating diagonal shear crack propagating from upper-left to lower-right, thereby achieving an exact match (Matched) at DS IV.

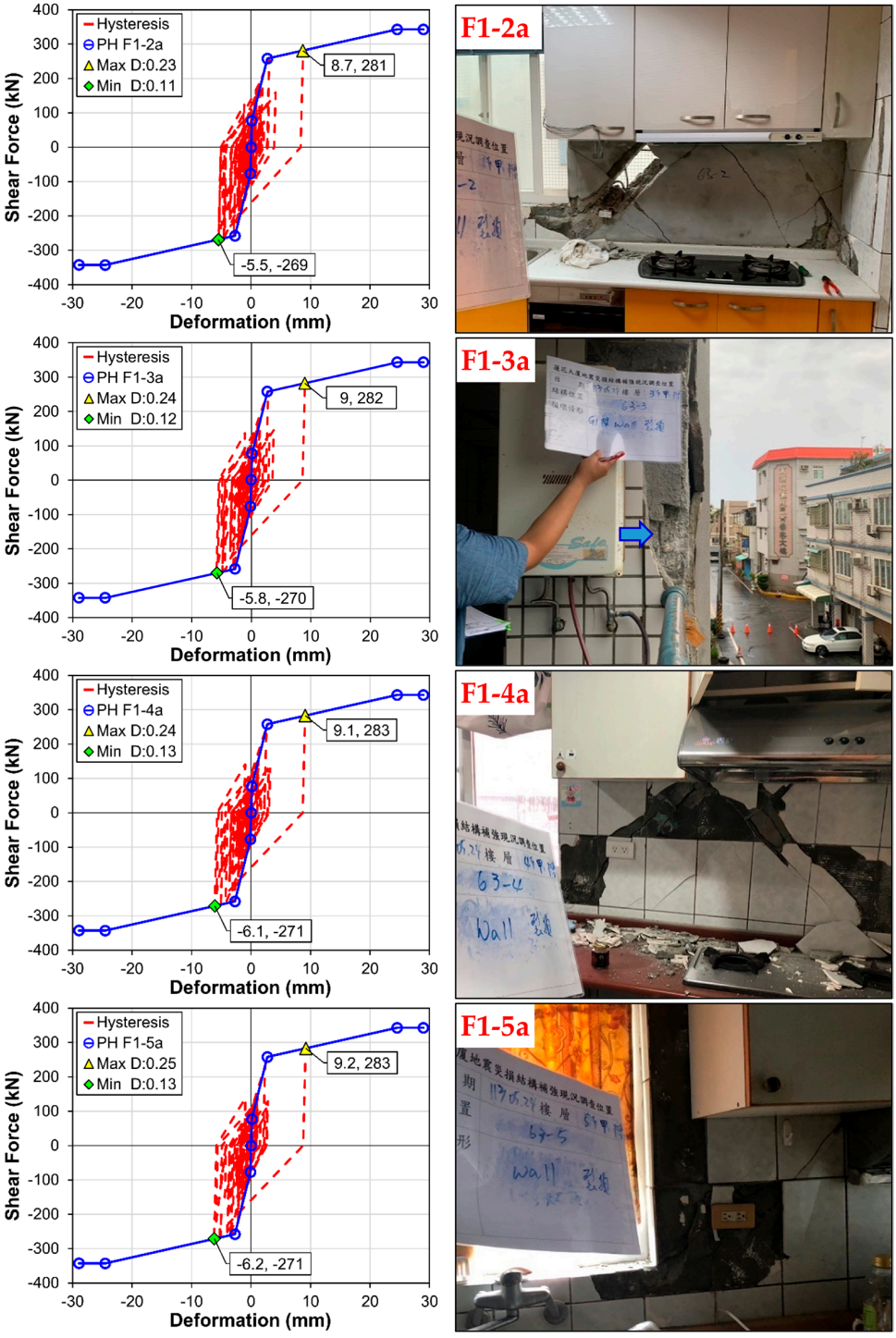

Figure 25. *Cont.*

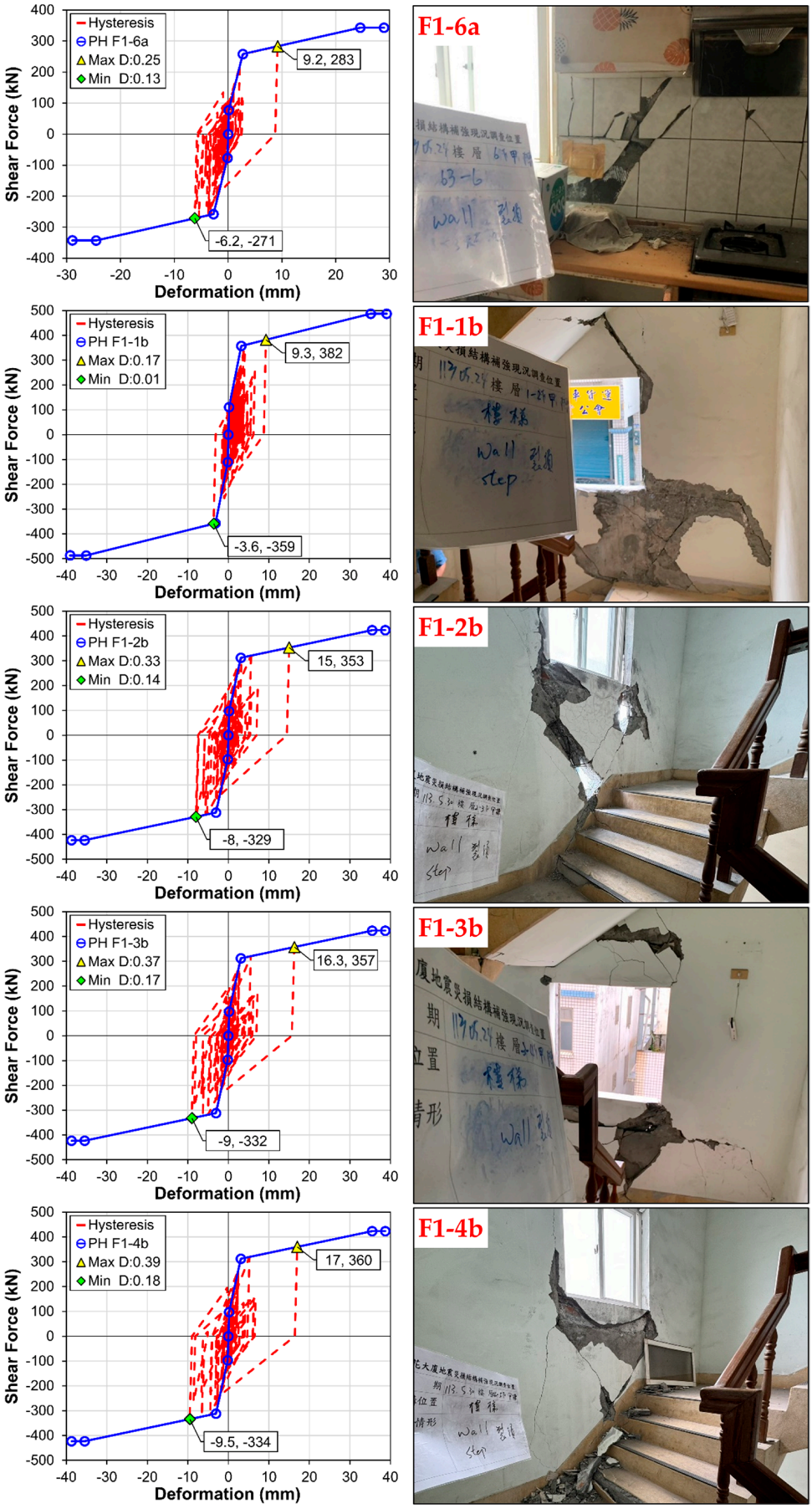

Figure 25. *Cont.*

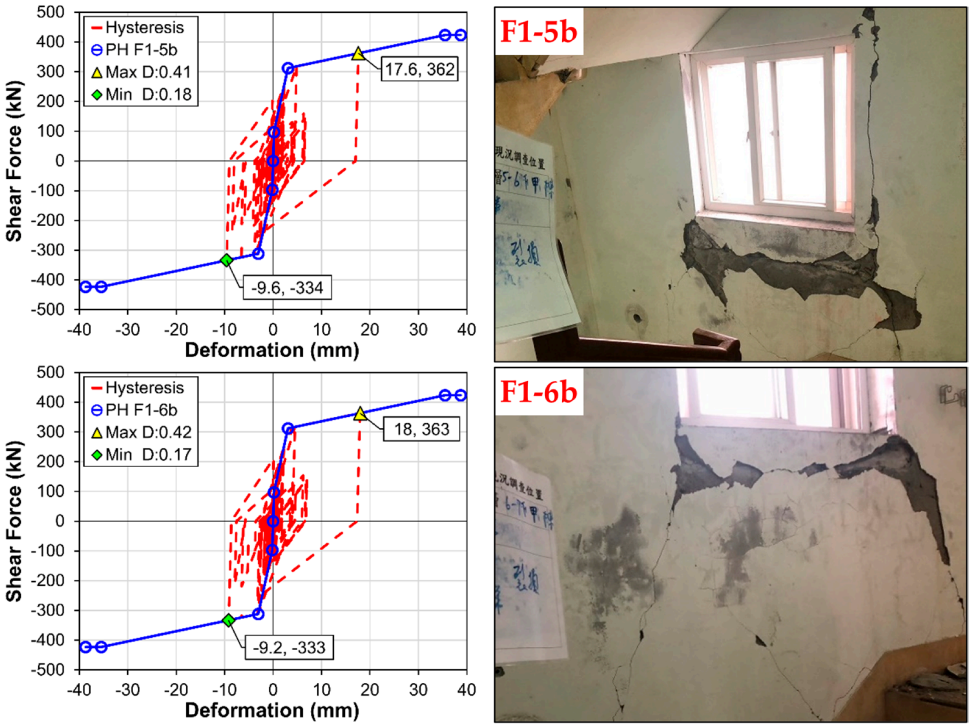

Figure 25. Cross-verification of numerical non-linear hysteretic loops against empirical post-earthquake damage states for critical wall elements in Frame 1. (The blue arrows in F1-3a indicate exposed reinforcing steel/exposed rebar).

Table 8. Comparison between analytical simulation results and field-observed damage states for Frame 2 wall components under HWA019 excitation.

Item	Analytical Simulation Results				Observed Field Damage Features					Correlation
	$\lvert V_{max} \rvert$ (kN)	$\lvert \Delta_{max} \rvert$ (mm)	D	Simulated DS	Crack Width (mm)	Cover Spalling	Rebar Exposure	Through-Wall Cracks	Observed DS	
F2-1a	1815	18.06	0.546	IV	>5	●	●	●	IV	Matched
F2-1b	442	2.68	0.371	III	3	◑	-	-	III	Matched
F2-2b	307	8.24	0.032	II	3	○	-	-	II	Matched
F2-3b	307	8.18	0.031	II	<1	-	-	-	II	Matched
F2-4b	306	7.76	0.025	II	<1	-	-	-	II	Matched
F2-5b	306	7.44	0.021	II	-	-	-	-	I	Minor Dev.
F2-6b	305	7.21	0.018	II	-	-	-	-	I	Minor Dev.

Note: Severity level of observed damage features: - = None; ○ = Slight; ◑ = Moderate; ● = Severe.

The adjacent ground-floor wall element F2-1b exhibited a lower response displacement ($\lvert \Delta_{max} \rvert$ = 2.68 mm) but reached a *D* index of 0.371 (Simulated DS III). This elevated ductility demand relative to its minor displacement is predominantly attributed to the limited deformation capacity inherent in its aspect ratio and structural detailing, aligning seamlessly with the observed moderate cover spalling and 3 mm cracking (Matched at DS III). Conversely, the upper-story shear walls (F2-2b through F2-6b) demonstrated restricted ductility mobilization, with *D* indices bounded between 0.018 and 0.032. While simulated responses placed these upper elements at Moderate damage (DS II), field reconnaissance documented a gradual transition from minor hairline cracking (<1 to 3 mm) down to negligible physical damage at the top levels (DS I).

Overall, 71.4% (5 out of 7) of the evaluated shear wall components in Frame 2 achieved an exact match between simulated and field-observed damage states, with the remaining upper-floor elements (F2-5b and F2-6b) showing only a minor one-class deviation (Minor Dev.). The relationship between the nonlinear hysteretic loops of each element and their observed failure topologies is illustrated in Figure 26. This high degree of quantitative

alignment further substantiates the efficacy of the SERCB-based plastic hinge formulation in capturing localized failure mechanisms and story-wise damage attenuation across different structural frames.

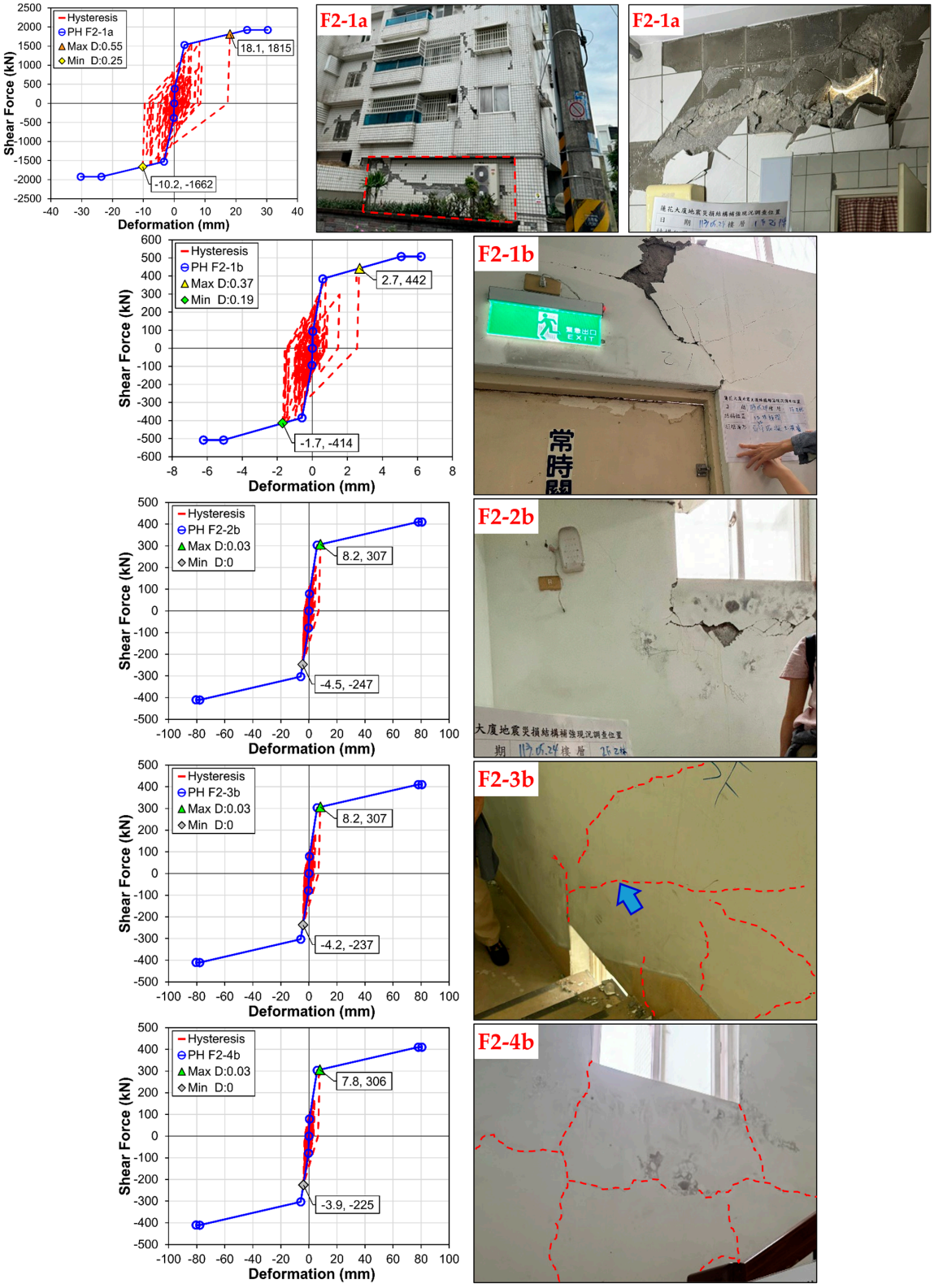

Figure 26. *Cont.*

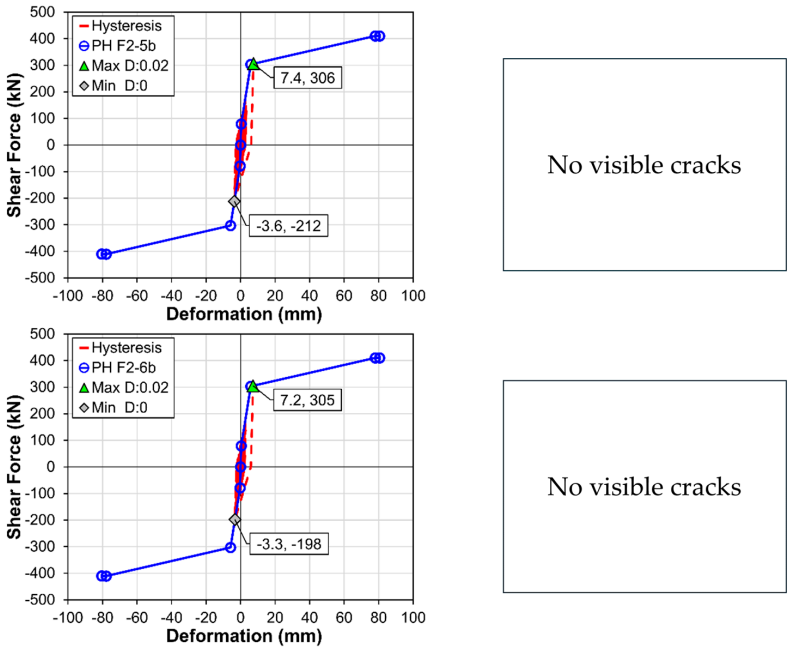

Figure 26. Cross-verification of numerical non-linear hysteretic loops against empirical post-earthquake damage states for critical wall elements in Frame 2. (The blue arrows indicate the specific crack locations, and the red dashed lines delineate the propagation paths of the cracks).

To evaluate the component-level damage, the calculated D indices of all column and beam plastic hinges from the 1st to the 6th stories were statistically summarized (Figure 27). The results indicate a low structural damage level. For the column components, 1767 plastic hinges remain within the elastic regime ($D = 0$), and only 14 (0.79%) hinges experience nonlinear demand with a D index within $0 < D \leq 0.2$. The maximum D index obtained among all columns is 0.0968, verifying that the vertical load-carrying elements sustain no failure.

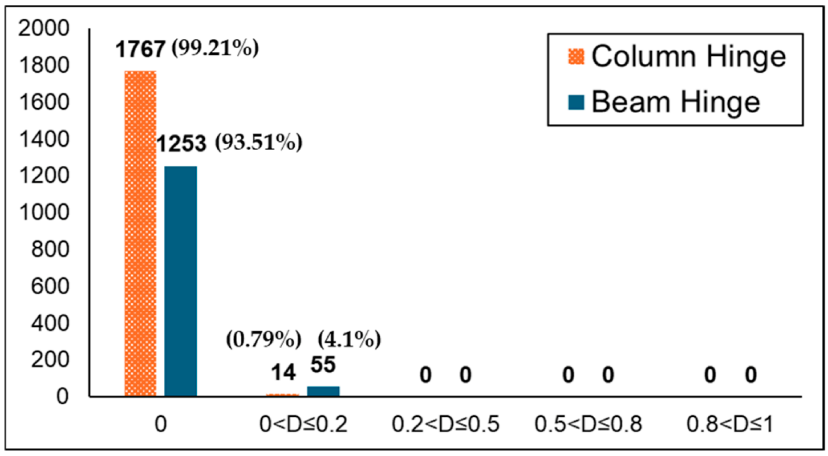

Figure 27. Statistical distribution of ductility development index (D) for column and beam plastic hinges (1F–6F).

On the other hand, the plastic hinges in beam components exhibit a higher degree of damage progression compared to those in columns. While 1253 (93.51%) beam hinges remain elastic ($D = 0$), 55 (4.1%) hinges fall within the range of $0 < D \leq 0.2$, with a maximum D index of 0.0973. No hinges enter higher damage states. This distribution demonstrates that plastic dissipation is concentrated within the flexural beams rather than the columns, conforming to the "strong column–weak beam" mechanism. The numerical

concentration of low D indices across both component types quantitatively confirms the damage state of the frame structure, directly correlating with the minor physical failures from the field reconnaissance.

5. Conclusions

5.1. Restatement of Research Aim

This study aimed to evaluate and quantitatively validate the dynamic seismic performance of a plan-irregular high-rise reinforced concrete (RC) building subjected to triaxial strong-motion records during the 2024 Hualien earthquake. By integrating mechanics-based SERCB plastic hinge constitutive models into nonlinear dynamic time-history analysis (NDTHA) via ETABS, this research sought to bridge the gap between numerical damage predictions and real-world post-earthquake field reconnaissance observations at a refined component level.

5.2. Summary of Key Findings

- Damage Spatial Distribution: Inelastic seismic demands were heavily concentrated in the lower-to-middle story shear walls (Stories 1–6). The lower wall system functioned as the primary lateral energy dissipation mechanism, preserving the integrity and gravity-load-carrying capacity of the main beam–column framework.
- Torsional Irregularity Effects: Plan asymmetry induced pronounced eccentric torsional behavior, amplifying lateral demands on perimeter frames. Outer Frame 1 reached Significant Damage (DS III, D = 0.2–0.4), while element F2-1a in Frame 2 sustained the most severe localized failure (DS IV, D = 0.546), characterized by penetrating diagonal shear cracking and rebar exposure.
- Quantitative Physical Validation: Component-level comparison confirmed strong agreement between analytical ductility indices (D) and physical damage features. Exact damage state matches (Matched) were achieved for 63.6% (7/11) of evaluated walls in Frame 1 and 71.4% (5/7) in Frame 2, with all remaining discrepancies bounded strictly within a minor one-class margin.

5.3. Main Contributions to Engineering Practice

- Bridge between Theory and Real-World Reconnaissance: This study extends conventional plastic hinge validation—traditionally restricted to isolated laboratory component tests—to a full-scale, real-world structural damage profile under triaxial strong motion.
- Standardized Post-Earthquake Assessment Template: The integrated methodology provides a reproducible framework for structural engineers to perform rapid safety evaluations and prioritize targeted retrofitting strategies in torsionally vulnerable RC structures.

5.4. Limitations and Future Directions

- Model Application Boundaries: The SERCB formulations and damage thresholds are tailored specifically for RC elements. Direct extension to steel, timber, or composite structural systems requires recalibrating material constitutive laws and backbone parameters against relevant experimental data.
- Discrete Bounding Effects: Using discrete D-index intervals for continuous physical damage may introduce minor one-class variations near threshold boundaries.
- Future Research Avenues: Future work will focus on expanding this methodology across RC structures with diverse story heights, varying plan layouts, and complex soil-

structure interaction (SSI) effects, as well as integrating machine-learning computer vision to automate field crack detection and damage mapping.

Author Contributions: Conceptualization, Y.-C.C. and Y.-C.S.; methodology, Y.-C.C. and K.-H.C.; software, Y.-C.C.; validation, Y.-C.C. and K.-H.C.; formal analysis, Y.-C.C.; investigation, Y.-C.C. and J.-S.L.; resources, J.-S.L. and K.-H.C.; data curation, Y.-C.C. and K.-H.C.; writing—original draft preparation, Y.-C.C.; writing—review and editing, Y.-C.S.; visualization, Y.-C.C.; supervision, Y.-C.S.; project administration, Y.-C.S. All authors have read and agreed to the published version of the manuscript.

Funding: This research received no external funding.

Data Availability Statement: The data used in this study are not publicly available due to confidentiality agreements. They contain sensitive information provided by third parties, including building documentation, field investigation records, and related structural details.

Acknowledgments: The authors acknowledge the assistance provided during the field investigation and the collection of relevant information for this study.

Conflicts of Interest: Author Jin-Sheng Lin was employed by the company Maoxin Engineering Consultants Co., Ltd. The remaining authors declare that the research was conducted in the absence of any commercial or financial relationships that could be construed as a potential conflict of interest.

References

1. Wang, Y.J.; Chan, C.H.; Lee, Y.T.; Ma, K.F.; Shyu, J.B.H.; Rau, R.J.; Cheng, C.T. Probabilistic seismic hazard assessment for Taiwan. *Terr. Atmos. Ocean. Sci.* **2016**, *27*, 325–340. [CrossRef]
2. Central Weather Administration (CWA). Seismological Database. Available online: https://scweb.cwa.gov.tw/en-us/earthquake/data (accessed on 20 April 2026).
3. Tsai, K.C.; Hsiao, C.P.; Bruneau, M. Overview of building damages in 921 Chi-Chi earthquake. *Earthq. Eng. Eng. Seismol.* **2000**, *2*, 93–108.
4. Su, N.; Lin, T.D.; Chai, H.W. Damage to structures and buildings from the Chi-Chi (Taiwan) earthquake. *Proc. Inst. Civ. Eng. Struct. Build.* **2002**, *152*, 51–56. [CrossRef]
5. Naeim, F.; Lew, M.; Huang, S.C.; Lam, H.K.; Carpenter, L.D. The performance of tall buildings during the 21 September 1999 Chi-Chi earthquake, Taiwan. *Struct. Des. Tall Build.* **2000**, *9*, 137–160. [CrossRef]
6. Henry, R.S.; Lee, B.Y.; McGuigan, D.; Finnegan, J.; Ashby, G. The 2016 Meinong Taiwan Earthquake: Learning from Earthquakes Report. *Bull. N. Z. Soc. Earthq. Eng.* **2017**, *50*, 436–468. [CrossRef]
7. Zepeda, D.; Hagen, G. Lessons learned from the 2016 Taiwan Mei-Nong earthquake. In Proceedings of the Structural Engineers Association of California (SEAOC) Convention, Maui, HI, USA, 12–15 October 2016; pp. 409–420.
8. Wang, X.; Nagano, M.; Si, H.; Chang, W.Y.; Kuo, C.H.; Lin, C.M. Questionnaire surveys on damages at high-rise buildings and synthesized near-fault long-period strong ground motions of the 2018 Hualien, Taiwan, earthquake. *Int. J. Disaster Risk Reduct.* **2021**, *61*, 102343. [CrossRef]
9. Ji, K.; Ren, Y.; Wen, R.; Kuo, C.H. Near-field velocity pulse-like ground motions on February 6, 2018 M_w 6.4 Hualien, Taiwan earthquake and structural damage implications. *Soil Dyn. Earthq. Eng.* **2019**, *126*, 105784. [CrossRef]
10. Central Weather Administration (CWA). Earthquake Report No. 019: April 3, 07:58, M_L 7.1, 13.6 km SSW of Hualien County. Available online: https://scweb.cwa.gov.tw/en-US/earthquake/Imgs/EE2024040307580971019 (accessed on 20 April 2026).
11. Chuang, M.C.; Tapia-Hernandez, E.; Chi, K.N.; Lin, H.Z.; Lin, J.L.; Guerrero, H.; Chou, C.C.; Ma, C.C. Field reconnaissance on seismic performance of buildings after the M_L 7.2 earthquake of April 3, 2024 in Hualien, Taiwan. *J. Build. Eng.* **2025**, *110*, 113076. [CrossRef]
12. Enokida, R.; Fukushima, Y.; Tang, C.H.; Pan, T.Y.; Kuo, C.L.; Ikago, K.; Izumi, T.; Kuriyama, S. Earthquake disaster resilience in Taiwan observed from the April 2024 M_L 7.1 Hualien earthquake. *Front. Built Environ.* **2025**, *11*, 1593942. [CrossRef]
13. Chopra, A.K. *Dynamics of Structures*, 3rd ed.; Pearson Education India: New Delhi, India, 2007.
14. Nascimbene, R. Numerical model of a reinforced concrete building: Earthquake analysis and experimental validation. *Period. Polytech. Civ. Eng.* **2015**, *59*, 521–530. [CrossRef]
15. Tu, Y.H.; Liu, T.W.; Ao, L.C.; Yeh, P.L. Nonlinear static seismic analysis and its validation using damage data from reinforced-concrete school buildings. In Proceedings of the 9th US National and 10th Canadian Conference on Earthquake Engineering 2010, Toronto, ON, Canada, 25–29 July 2010; pp. 2880–2889.

16. Yang, H.; Wang, H.; Jeremić, B. Numerical modeling and validation of earthquake soil structure interaction: A 12-story building in Ventura, California. *Front. Built Environ.* **2023**, *9*, 1249550. [CrossRef]
17. Cosgun, T.; Sayin, B.; Gunes, B.; Mangir, A. Retrofitting technique effectiveness and seismic performance of multi-rise RC buildings: A case study. *Case Stud. Constr. Mater.* **2022**, *16*, e00931. [CrossRef]
18. Peker, F.U.; Yuzbasi, J.; Isik, E.; Avcil, F.; Buyuksarac, A. Seismic performance assessment and strengthening of a residential RC building damaged in the 2023 Türkiye earthquakes: A case study. *Sci. Rep.* **2026**, *16*, 23737. [CrossRef]
19. Kocakaplan Sezgin, S.; Sakcalı, G.B.; Özen, S.; Yıldırım, E.; Avcı, E.; Bayhan, B.; Çağlar, N. Reconnaissance Report on Damage Caused by the February 6, 2023, Kahramanmaraş Earthquakes in Reinforced-Concrete Structures. *J. Build. Eng.* **2024**, *89*, 109200. [CrossRef]
20. Aguayo, R.; Carvallo, J.; Vielma, J.C. Evaluating seismic performance in reinforced concrete buildings with complex shear walls: A focus on a residential case in Chile. *Buildings* **2024**, *14*, 761. [CrossRef]
21. Blasi, G.; Scarlino, A.S.; Chirivì, S.; Perrone, D.; Aiello, M.A. Seismic Response of Irregular RC Buildings Designed for Gravity and Seismic Loads. *Bull. Earthq. Eng.* **2024**, *22*, 5231–5257. [CrossRef]
22. Sönmez, E.; Eryılmaz Yıldırım, M.; Aydın, M.F.; Köroğlu, F.B. Seismic Performance Assessment of Structural Systems in the Aftermath of the 2023 Kahramanmaraş Earthquakes: Observations and Fragility Analyses. *Earthq. Spectra* **2025**, *41*, 198–218. [CrossRef]
23. Tan, M.; Avşar, Ö.; Yıldızhan, F.; Atmaca, N. Effect of Infill Walls on the Seismic Performance of a Severely Damaged Substandard RC Building during the February 6, 2023, Kahramanmaras Earthquake Sequence. *Eng. Fail. Anal.* **2025**, *169*, 109117. [CrossRef]
24. Geological Survey and Mining Management Agency (GSMMA); Ministry of Economic Affairs (MOEA). Geology Cloud Value-Added Application Platform. Available online: https://www.geologycloud.tw/map/zh-tw (accessed on 20 April 2026).
25. Geological Survey and Mining Management Agency (GSMMA); Ministry of Economic Affairs (MOEA). Engineering Geological Investigation Database. Available online: https://geotech.gsmma.gov.tw/imoeagis/Home/Map# (accessed on 20 April 2026).
26. Construction and Disaster Protection Division, National Land Management Agency (NLMA). *Building Seismic Design Code and Commentary of Taiwan*; Ministry of the Interior: Taipei, Taiwan, 2024.
27. Sung, Y.C.; Liu, K.Y.; Su, C.K.; Tsai, I.C.; Chang, K.C. A study on pushover analyses of reinforced concrete columns. *Struct. Eng. Mech.* **2005**, *21*, 35–52. [CrossRef]
28. Lai, M.C.; Sung, Y.C. A study on pushover analysis of frame structure infilled with low-rise reinforced concrete wall. *J. Mech.* **2008**, *24*, 437–449. [CrossRef]
29. Ministry of the Interior (MOI). *Emergency Assessment Form for Hazardous Buildings After Disasters*; Order No. 1120805057; Ministry of the Interior: Taipei, Taiwan, 2023.
30. Park, Y.J.; Ang, A.H.S. Mechanistic seismic damage model for reinforced concrete. *J. Struct. Eng.* **1985**, *111*, 722–739. [CrossRef]
31. Su, J.; Dhakal, R.P.; Wang, J. Fiber-based damage analysis of reinforced concrete bridge piers. *Soil Dyn. Earthq. Eng.* **2017**, *96*, 13–34. [CrossRef]

Disclaimer/Publisher's Note: The statements, opinions and data contained in all publications are solely those of the individual author(s) and contributor(s) and not of MDPI and/or the editor(s). MDPI and/or the editor(s) disclaim responsibility for any injury to people or property resulting from any ideas, methods, instructions or products referred to in the content.